

Analysis of (sub-)Riemannian PDE-G-CNNs

Gijs Bellaard, Daan Bon, Gautam Pai, Bart Smets and Remco Duits

Department of Mathematics and Computer Science, CASA, Eindhoven University of Technology, Eindhoven, The Netherlands .

Abstract

Group equivariant convolutional neural networks (G-CNNs) have been successfully applied in geometric deep-learning. Typically, G-CNNs have the advantage over CNNs that they do not waste network capacity on training symmetries that should have been hard-coded in the network. The recently introduced framework of PDE-based G-CNNs (PDE-G-CNNs) generalize G-CNNs. PDE-G-CNNs have the core advantages that they simultaneously 1) reduce network complexity, 2) increase classification performance, 3) provide geometric network interpretability. Their implementations solely consist of linear and morphological convolutions with kernels.

In this paper we show that the previously suggested approximative morphological kernels do not always approximate the exact kernels accurately. More specifically, depending on the spatial anisotropy of the Riemannian metric, we argue that one must resort to sub-Riemannian approximations. We solve this problem by providing a new approximative kernel that works regardless of the anisotropy. We provide new theorems with better error estimates of the approximative kernels, and prove that they all carry the same reflectional symmetries as the exact ones.

We test the effectiveness of multiple approximative kernels within the PDE-G-CNN framework on two datasets, and observe an improvement with the new approximative kernel. We report that the PDE-G-CNNs again allow for a considerable reduction of network complexity while having a comparable or better performance than G-CNNs and CNNs on the two datasets. Moreover, PDE-G-CNNs have the advantage of better geometric interpretability over G-CNNs, as the morphological kernels are related to association fields from neurogeometry.

Keywords: Convolutional neural networks, Scale space theory, Geometric deep learning, Morphological convolutions, PDEs, Riemannian Geometry, sub-Riemannian Geometry

1 Introduction

Many classification, segmentation, and tracking tasks in computer vision and digital image processing require “symmetry”. Think for example of image classification. If one rotates, reflects, or translates an image the classification stays the same. We say that an ideal image classification is *invariant* under these symmetries. A slightly different situation is image segmentation. In this case

if the input image is in some way changed the output should change accordingly. Therefore, an ideal image segmentation is *equivariant* with respect to these symmetries.

A lot of computer vision and image processing problems are currently being tackled with *neural networks* (NNs). It is desirable to design neural networks in such a way that they respect the symmetries of the problem, i.e. make them invariant or equivariant. Think for example of a neural network that detects cancer cells. It would be disastrous if,

by for example slightly translating an image, the neural network would give totally different diagnoses, even though the input is essentially the same.

One way to make the networks equivariant or invariant is to simply train them on more data. One could take the training dataset and augment it with translated, rotated and reflected versions of the original images. This approach however is undesirable: invariance and equivariance is still not guaranteed and training takes longer. It is better if the networks are *inherently* invariant or equivariant by design. This avoids a waste of network-capacity, avoids creating local minima, guarantees invariance or equivariance, and increases performances, see for example [8].

More specifically, many computer vision and image processing problems are tackled with *convolutional neural networks* (CNNs) [38–40]. Convolution neural networks have the property that they inherently respect, to some degree, translation symmetries. CNNs do not however take into account rotational or reflection symmetries. Cohen and Welling introduced *group equivariant convolutional neural networks* (G-CNNs) in [18] and designed a classification network that is inherently invariant under 90 degree rotations, integer translations and vertical/horizontal reflections. Much work is being done on invariant/equivariant networks that exploit inherent symmetries, a non-exhaustive list is [5, 8–10, 16, 17, 19, 20, 28, 32, 37, 42, 43, 47, 49, 53–59]. The idea of including symmetries into the design of neural networks is called ‘Geometric Deep Learning’ in [13].

In [50] partial differential equation (PDE) based G-CNNs are presented, aptly called PDE-G-CNNs. In fact, G-CNNs are shown to be a *special case* of PDE-G-CNNs (if one restricts the PDE-G-CNNs only to convection, using many transport vectors [50, Sec.6]). With PDE-G-CNNs the usual non-linearities that are present in current networks, such as the ReLU activation function and max-pooling, are replaced by solvers for specifically chosen non-linear evolution PDEs. Figure 1 illustrates the difference between a traditional CNN layer and a PDE-G-CNN layer.

The PDEs that are used in PDE-G-CNNs are not chosen arbitrarily: they come directly from the world of geometric image analysis, and thus their effects are geometrically interpretable. This gives

PDE-G-CNNs an improvement in interpretability over traditional CNNs. Specifically, the PDEs considered are diffusion, convection, dilation and erosion. These 4 PDEs correspond with the common notions of smoothing, shifting, max pooling, and min pooling. They are solved by linear convolutions, resamplings, and so-called *morphological convolutions*. Figure 2 illustrates the basic building block of a PDE-G-CNN.

One shared property of G-CNNs and PDE-G-CNNs is that the input data usually needs to be *lifted* to a higher dimensional space. Take for example the case of image segmentation with a convolution neural network where we model/idealize the images as function on \mathbb{R}^2 . If we keep the data as functions on \mathbb{R}^2 and want the convolutions within the network to be equivariant, then the only possible ones that are allowed are with isotropic kernels, [23, p.258]. This type of shortcoming generalizes to other symmetry groups as well [5, Thm.1]. One can imagine that this is a constraint too restrictive to work with, and that is why we lift the image data.

Within the PDE-G-CNN framework the input images are considered real-valued functions on \mathbb{R}^d , the desired symmetries are represented by the Lie group of roto-translations $SE(d)$, and the data is lifted to an orientation score [24] defined on the homogeneous space of d dimensional positions and orientations \mathbb{M}_d . It is on this higher dimensional space on which the evolution PDEs are defined, and the effects of diffusion, dilation, and erosion are completely determined by the Riemannian metric tensor field \mathcal{G} that is chosen on \mathbb{M}_d . If this Riemannian metric tensor field \mathcal{G} is left-invariant, the overall processing is equivariant, this follows directly by combining techniques in [24, Thm. 21, ch:4], [26, Lemma 3, Thm. 4].

The Riemannian metric tensor field \mathcal{G} we will use in this article is left-invariant and determined by three nonnegative parameters: w_1 , w_2 , and w_3 . The definition can be found in the preliminaries, Section 2 Equation (8). It is exactly these three parameters that during the training of a PDE-G-CNN are optimized. Intuitively, the parameters correspondingly regulate the cost of main spatial, lateral spatial, and angular motion. An important quantity in the analysis of this paper is the *spatial anisotropy* $\zeta := \frac{w_1}{w_2}$, as will become clear later.

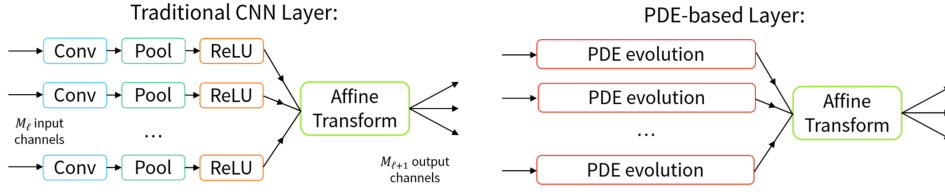


Fig. 1: The difference between a traditional CNN layer and a PDE-G-CNN layer. In contrast to traditional CNNs, the layers in a PDE-G-CNN do not depend on ad-hoc non-linearities like ReLU's, and are instead implemented by morphological convolutions that solve the erosion and dilation PDEs.

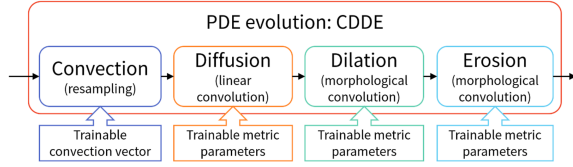


Fig. 2: Overview of a PDE-G-CNN layer. The linear parts are solved by linear group convolutions with a certain kernel [50], and the non-linear parts are solved by morphological convolutions (5) with a morphological kernel (1).

In this article we only consider the 2 dimensional case, i.e. $d = 2$. In this case the elements of both \mathbb{M}_2 and $SE(2)$ can be represented by three real numbers: $(x, y, \theta) \in \mathbb{R}^2 \times [0, 2\pi)$. In the case of \mathbb{M}_2 the x and y represent a position and θ represents an orientation. Throughout the article we take $\mathbf{p}_0 := (0, 0, 0) \in \mathbb{M}_2$ as our *reference point* in \mathbb{M}_2 . In the case of $SE(2)$ we have that x and y represent a translation and θ a rotation.

As already stated, within the PDE-G-CNN framework images are lifted to the higher dimensional space of positions and orientations \mathbb{M}_d . There are a multitude of ways of achieving this, but there is one very natural way to do it: the *orientation score transform* [4, 24, 25, 34]. In this transform we pick a point $(x, y) \in \mathbb{R}^2$ in an image and determine how good a certain orientation $\theta \in [0, 2\pi)$ fits the chosen point. In Figure 3 an example of an orientation score is given. For this article it is not necessary to know how such a transform exactly works, only that it exists.

The inspiration for using orientation scores comes from biology. The Nobel laureates Hubel and Wiesel found that many cells in the visual cortex of cats have a preferred orientation [12, 36]. Moreover, a neuron that fires for a specific orientation excites neighboring neurons that have

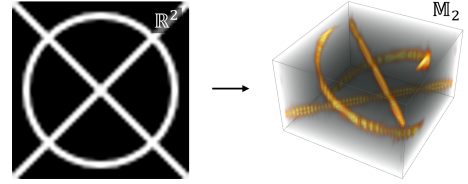


Fig. 3: An example of an image together with its orientation score. We can see that the image, a real-valued function on \mathbb{R}^2 , is lifted to an orientation score, a real-valued function on \mathbb{M}_2 . Notice that the lines that are crossing in the left image are disentangled in the orientation score.

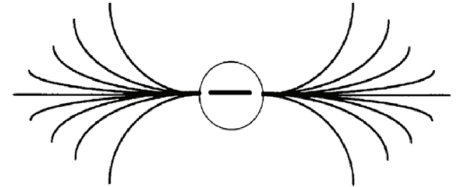


Fig. 4: Association field lines from neurogeometry [44, Fig.43], [31, Fig.16]. Such association field lines can be well approximated by spatially projected sub-Riemannian geodesics in \mathbb{M}_2 [2, 15, 33, 44], [22, Fig.17].

an “aligned” orientation. Petitot and Citti-Sarti proposed a model [15, 44] for the distribution of the orientation preference and this excitation of neighbors based on sub-Riemannian geometry on \mathbb{M}_2 . They relate the phenomenon of preference of aligned orientations to the concept of *association fields* [31], which model how a specific local orientation puts expectations on surrounding orientations in human vision. Figure 4 provides an impression of such an association field.

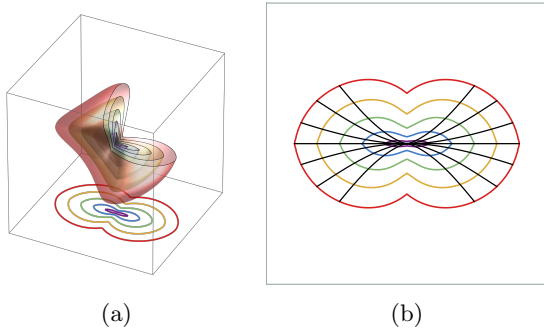


Fig. 5: A visualization of the exact Riemannian distance d , and its relation with association fields. In 5a we see isocontours of $d(\mathbf{p}_0, \cdot)$ in \mathbb{M}_2 , and on the bottom we see the min-projection over θ of these contours (thus we selected the minimal ending angle in contrast to Figure 4). The domain of the plot is $[-3, 3]^2 \times [-\pi, \pi] \subset \mathbb{M}_2$. The chosen contours are $d = 0.5, 1, 1.5, 2$, and 2.5 . The metric parameters are $(w_1, w_2, w_3) = (1, 64, 1)$. Due to the very high spatial anisotropy we approach the sub-Riemannian setting. In 5b we see the same min-projection together with some corresponding spatially projected geodesics.

As shown in [22, Fig.17] association fields are closely approximated by (projected) sub-Riemannian geodesics in \mathbb{M}_2 for which optimal synthesis has been obtained by Sachkov and Moiseev [41, 46]. Furthermore, in [27] it is shown that Riemannian geodesics in \mathbb{M}_2 converge to the sub-Riemannian geodesics by increasing the spatial anisotropy ζ of the metric. This shows that in practice one can approximate the sub-Riemannian model by Riemannian models. Figure 5 shows the relation between association fields and sub-Riemannian geometry in \mathbb{M}_2 .

The relation between association fields and Riemannian geometry on \mathbb{M}_2 directly extends to a relation between dilation/erosion and association fields. Namely, performing dilation on an orientation score in \mathbb{M}_2 is similar to extending a line segment along its association field lines. Similarly, performing erosion is similar to sharpening a line segment perpendicular to its association field lines. This makes dilation/erosion the perfect candidate for a task such as *line completion*.

In the line completion problem the input is an image containing multiple line segments, and the desired output is an image of the line that is

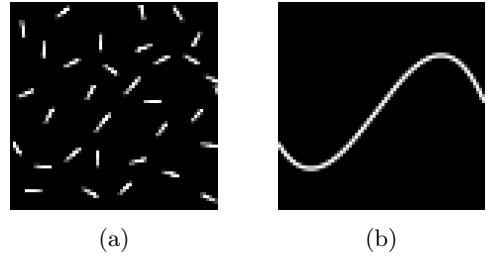


Fig. 6: One sample of the Lines dataset. In 6a we see the input, in 6b the perceived curve that we consider as ground-truth (as the input is constructed by interrupting the ground-truth line and adding random local orientations).

“hidden” in the input image. Figure 6 shows such an input and desired output. This is also what David Field et al. studied in [31]. We anticipate that PDE-G-CNNs outperform classical CNNs in the line completion problem due to PDE-G-CNNs being able to dilate and erode. To investigate this we programmatically made a dataset called “Lines” consisting of grayscale images of 64×64 pixels, together with their ground-truth line completion. In Figure 7 a complete abstract overview of the architecture of a PDE-G-CNN performing line completion is visualized. Figure 8 illustrates how a PDE-G-CNN incrementally completes a line throughout the PDE layers.

In Proposition 1 we show that solving the dilation and erosion PDEs can be done by performing a morphological convolution with a *morphological kernel* $k_t^\alpha : \mathbb{M}_2 \rightarrow \mathbb{R}_{\geq 0}$, that is easily expressed in the Riemannian distance $d = d_G$ on the manifold:

$$k_t^\alpha(\mathbf{p}) = \frac{t}{\beta} \left(\frac{d_G(\mathbf{p}_0, \mathbf{p})}{t} \right)^\beta. \quad (1)$$

Here $\mathbf{p}_0 = (0, 0, 0)$ is our reference point in \mathbb{M}_2 , and time $t > 0$ controls the amount of erosion and dilation. Furthermore, $\alpha > 1$ controls the “softness” of the max and min-pooling, with $\frac{1}{\alpha} + \frac{1}{\beta} = 1$. Erosion is done through a direct morphological convolution (5) with this specific kernel. Dilation is solved in a slightly different way but again with the same kernel (Proposition 1 in Section 3 will explain the details).

And this is where a problem arises: calculating the exact distance d on \mathbb{M}_2 required in (1) is computationally expensive [7]. To alleviate this issue

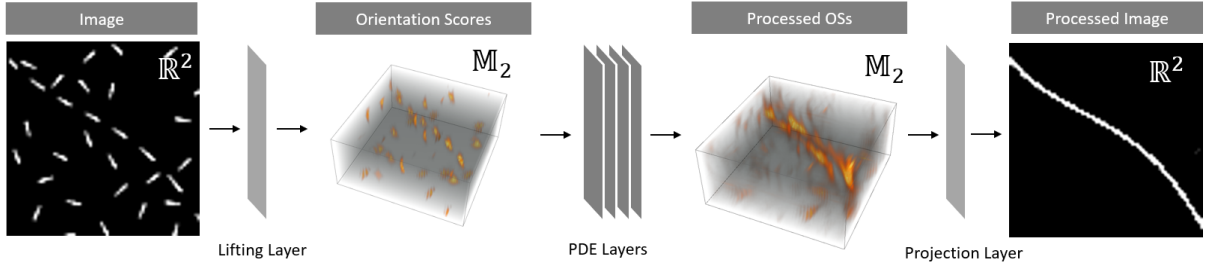


Fig. 7: The overall architecture for a PDE-G-CNN performing line completion on the Lines data set. Note how the input image is lifted to an orientation score that lives in the higher dimensional space \mathbb{M}_2 , run through PDE-G-CNN layers, and afterwards projected down back to \mathbb{R}^2 .

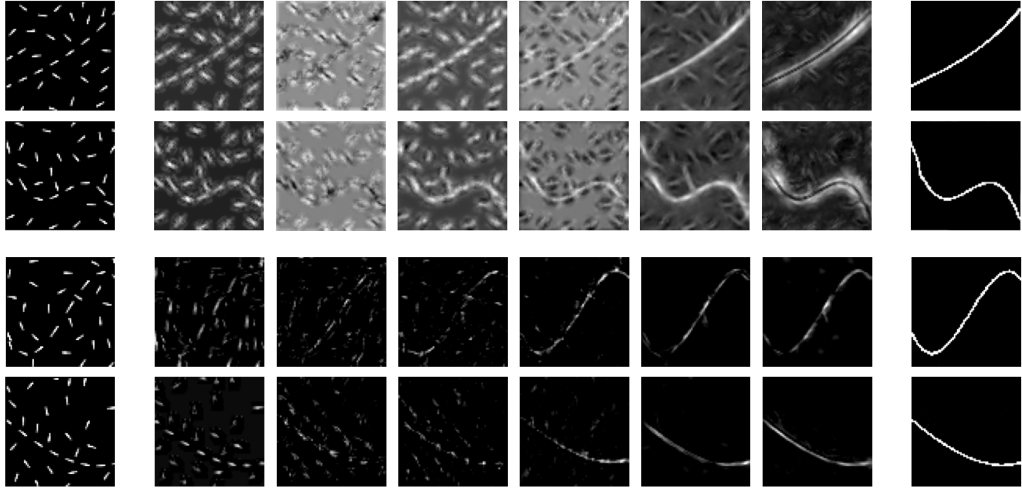


Fig. 8: Visualization of how a PDE-G-CNN and CNN incrementally complete a line throughout their layers. The first two rows are of a PDE-G-CNN, the second two rows of a CNN. The first column is the input, the last column the output. The intermediate columns are a selection of feature maps from the respective layer within the network. Within the feature maps of the PDE-G-CNN association fields from neurogeometry [31, 44] become visible as network depth increases. Such merging of association fields is not visible in the feature maps of the CNN. This observation is consistent throughout different inputs.

we resort to estimating the true distance d with computationally efficient approximative distances, denoted throughout the article by ρ . We then use such a distance approximation within (1) to create a corresponding approximative morphological kernel, and in turn use this to efficiently calculate the effect of dilation and erosion.

In [50] one such distance approximation is used: the *logarithmic distance estimate* ρ_c which uses the logarithmic coordinates c^i (13). In short, $\rho_c(\mathbf{p})$ is equal to the Riemannian length of the

exponential curve that connects \mathbf{p}_0 to \mathbf{p} . The formal definition will follow in Section 4. In Figure 9 an impression is given of ρ_c .

Clearly, an error is made when the effect of erosion and dilation is calculated with an approximative morphological kernel. As a morphological kernel is completely determined by its corresponding (approximative) distance, it follows that one can analyse the error by analyzing the difference between the exact distance d and approximative distance ρ that is used.

Despite showing in [50] that $d \leq \rho_c$ no concrete bounds are given, apart from the asymptotic

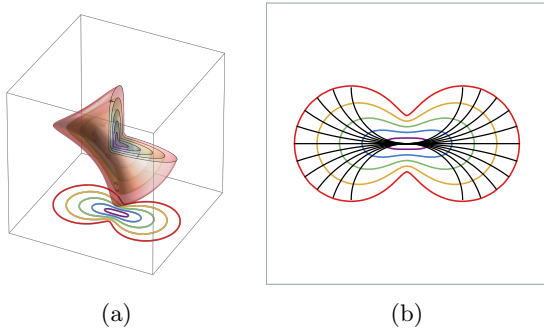


Fig. 9: A visualization of ρ_c , similar to Figure 5. In 9a we see multiple contours of ρ_c , and on the bottom we see the min-projection over θ . The metric parameters are $(w_1, w_2, w_3) = (1, 4, 1)$. In 9b we see the same min-projection together with some corresponding spatially projected exponential curves. Note the similarity to Figure 4.

$\rho_c^2 \leq d^2 + \mathcal{O}(d^4)$. This motivates us to do a more in-depth analysis on the quality of the distance approximations.

We introduce a variation on the logarithmic estimate ρ_c called the *half-angle distance estimate* ρ_b , and analyse that. The half-angle approximation uses not the logarithmic coordinates but half-angle coordinates b^i . The definition of these is also given later (34). In practice ρ_c and ρ_b do not differ much, but analysing ρ_b is much easier!

The main theorem of the paper, Theorem 1, collects new theoretical results that describe the quality of using the half-angle distance approximation ρ_b for solving dilation and erosion in practice. It relates the approximative morphological kernel k_b corresponding with ρ_b , to the exact kernel k (1).

Both the logarithmic estimate ρ_c and half-angle estimate ρ_b approximate the true Riemannian distance d quite well in certain cases. One of these cases is when the Riemannian metric has a low spatial anisotropy ζ . We can show this visually by comparing the isocontours of the exact and approximative distances. However, interpreting and comparing these surfaces can be difficult. This is why we have decided to additionally plot multiple θ -isocontours of these surfaces. In Figure 10 one such plot can be seen, and illustrates how it must be interpreted.

In Table 1 a spatially isotropic $\zeta = 1$ and low-anisotropic case $\zeta = 2$ is visualized. Note that ρ_b approximates d well in these cases. In fact, ρ_b is

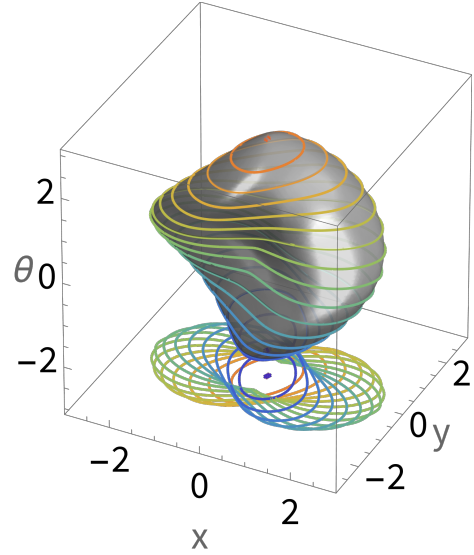


Fig. 10: In grey the isocontour $d = 2.5$ is plotted. The metric parameters are $(w_1, w_2, w_3) = (1, 8, 1)$. For $\theta = k\pi/10$ with $k = -10, \dots, 10$ the isocontours are drawn and projected onto the bottom of the figure. The same kind of visualizations are used in Tables 1 and 2.

exactly equal to the true distance d in the spatially isotropic case, which *is not true* for ρ_c .

Both the logarithm and half-angle approximation fail specifically in the high spatial anisotropy regime. For example when $\zeta = 8$. The first two columns of Table 2 show that, indeed, ρ_b is no longer a good approximation of the exact distance d . For this reason we introduce a novel *sub-Riemannian* distance approximations $\rho_{b, sr}$, which is visualized in the third column of Table 2.

Finally, we propose an approximative distance ρ_{com} that carefully combines the Riemannian and sub-Riemannian approximations into one. This combined approximation automatically switches to the estimate that is more appropriate depending on the spatial anisotropy, and hence covers both the low and high anisotropy regimes. Using the corresponding morphological kernel of ρ_{com} to solve erosion and dilation we obtain more accurate (and still tangible) solutions of the non-linear parts in the PDE-G-CNNs.

For every distance approximation (listed in Section 4) we perform an empirical analysis in Section 7 by seeing how the estimate changes the

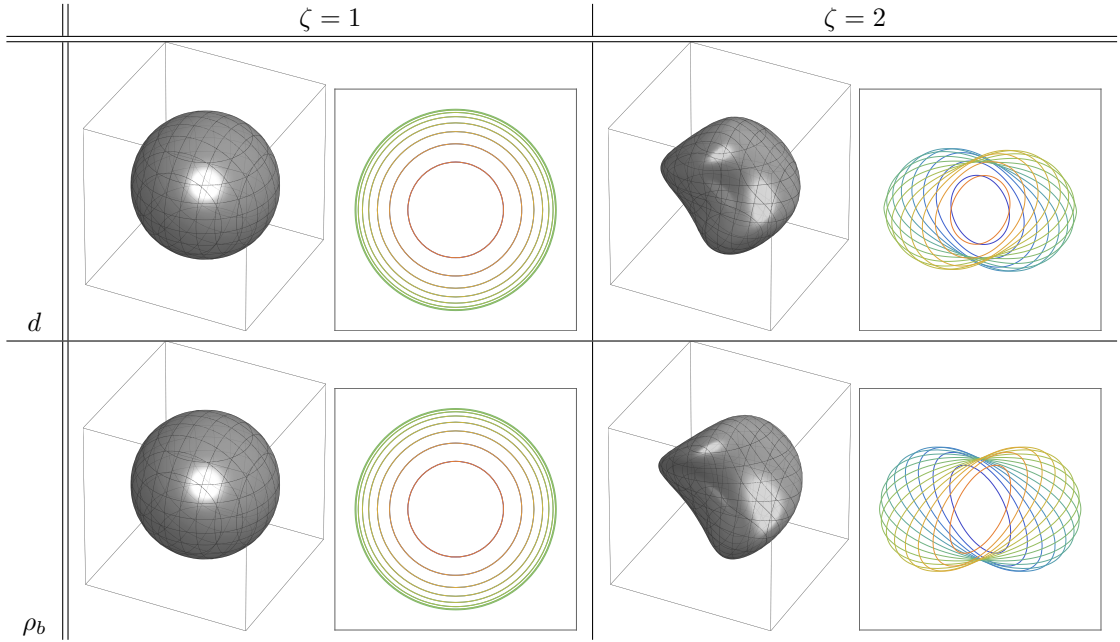


Table 1: The balls of the exact distance d and approximative distance ρ_b in the isotropic and low anisotropic case. The radius of the balls is set to $r = 2.5$. The domain of the plots is $[-3, 3] \times [-3, 3] \times [-\pi, \pi)$. We fix $w_1 = w_3 = 1$ throughout the plots and vary w_2 . For $\theta = k\pi/10$ with $k = -10, \dots, 10$ the isocontours are drawn, similar to Figure 10.

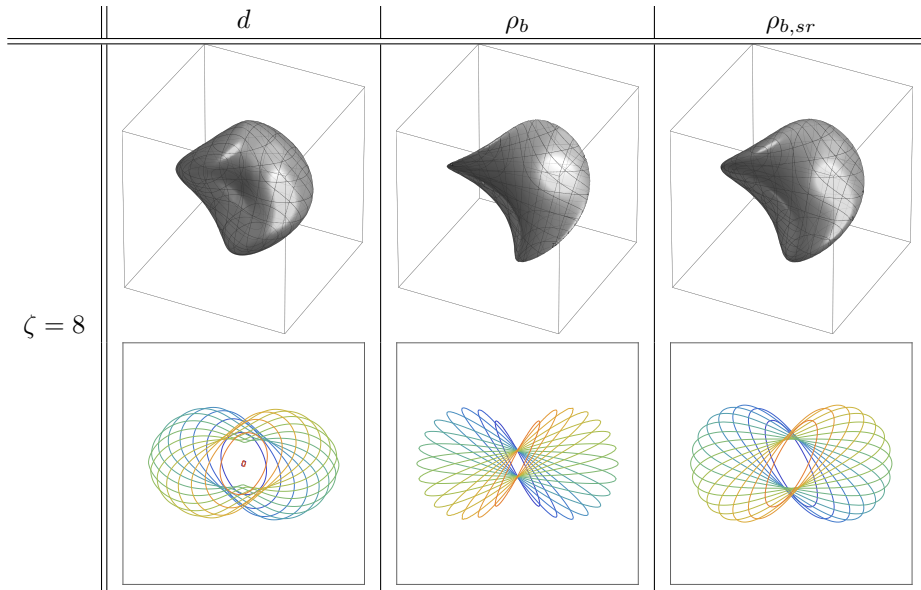


Table 2: The same as Table 1 but in the high spatially anisotropic case. Alongside the approximation ρ_b the sub-Riemannian distance approximation $\rho_{b, sr}$ is plotted with $\nu = 1.6$. We see that the isocontours of ρ_b are too “thin” compared to the isocontours of d . The isocontours of $\rho_{b, sr}$ are better in this respect.

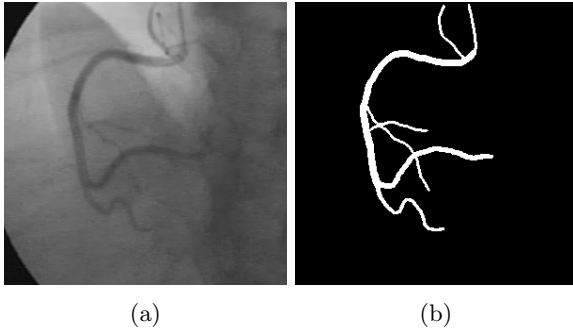


Fig. 11: One sample of the DCA1 dataset. In 11a we see a coronary angiogram, in 11b the ground-truth given by an expert cardiologist.

performance of the PDE-G-CNNs when applied to two datasets: the Lines dataset and DCA1 dataset.

The DCA1 dataset is a publicly available database “consisting of 130 X-ray coronary angiograms, and their corresponding ground-truth image outlined by an expert cardiologist” [14]. One such angiogram and ground-truth can be seen in Figure 11.

1.1 Contributions

In Proposition 1 we summarize how the nonlinear units in PDE-G-CNNs (described by morphological PDEs) are solved using morphological kernels and convolutions, which provides sufficient and essential background for the discussions and results in this paper.

The key contributions of this article are:

- Theorem 1 summarizes our mathematical analysis of the quality of the half-angle distance approximation ρ_b and its corresponding morphological kernel k_b in PDE-G-CNNs. We do this by comparing k_b to the exact morphological kernel k . Globally, one can show that they both carry the same symmetries, and that for low spatial anisotropies ζ they are almost indistinguishable. Furthermore, we show that locally both kernels are similar through an upper bound on the relative error. This improves upon results in [50, Lem.20].
- Table 2 demonstrates qualitatively that ρ_b becomes a poor approximation when the spatial anisotropy is high $\zeta \gg 1$. In Corollary 4 we underpin this theoretically and in Section 7.1 we validate this observation numerically. This

motivates the use of a sub-Riemannian approximation when ζ is large.

- In Section 4 we introduce and derive a novel sub-Riemannian distance approximation ρ_{sr} , that overcomes difficulties in previous existing sub-Riemannian kernel approximations [6]. Subsequently, we propose our approximation ρ_{com} that combines the Riemannian and sub-Riemannian approximations into one that automatically switches to the approximation that is more appropriate depending on the metric parameters.
- Figures 16 and 18 shows that PDE-G-CNNs perform just as well as, and sometimes better than, G-CNNs and CNNs on the DCA1 and Lines dataset, while having the least amount of parameters. Figures 17 and 19 depict an evaluation of the performance of PDE-G-CNNs when using the different distance approximations, again on the DCA1 and Lines dataset. We observe that the new kernel $\rho_{b,com}$ provides best results.

In addition, Figures 4, 7 and 8 show a connection between the PDE-G-CNN framework with the theory of association fields from neurogeometry [31, 44]. Thereby, PDE-G-CNNs reveal improved geometrical interpretability, in comparison to existing convolution neural networks.

1.2 Structure of the Article

In Section 2 a short overview of the necessary preliminaries is given. Section 3 collects some known results on the exact solution of erosion and dilation on the homogeneous space of two-dimensional positions and orientations \mathbb{M}_2 , and motivates the use of morphological kernels. In Section 4 all approximative distances are listed. The approximative distances give rise to corresponding approximative morphological kernels. The main theorem of this paper can be found in Section 5 and consist of three parts. The proof of these three parts can be found in the subsections of Section 6. The main theorem mostly concerns itself with the analysis of one specific approximative morphological kernel k_b . Experiments with various approximative kernels are done and the result can be found in Section 7. Finally, we end the paper with a conclusion in Section 8.

2 Preliminaries

Coordinates on $SE(2)$ and \mathbb{M}_2 . Let $G = SE(2) = \mathbb{R}^2 \rtimes SO(2)$ be the two-dimensional rigid body motion group. We identify elements $g \in G$ with $g \equiv (x, y, \theta) \in \mathbb{R}^2 \times \mathbb{R}/(2\pi\mathbb{Z})$, via the isomorphism $SO(2) \cong \mathbb{R}/(2\pi\mathbb{Z})$.

For $g_1 = (x_1, y_1, \theta_1)$, $g_2 = (x_2, y_2, \theta_2) \in SE(2)$ we have the group product

$$\begin{aligned} g_1 g_2 &:= (x_1 + x_2 \cos \theta - y_2 \sin \theta, \\ &\quad y_1 + x_2 \sin \theta + y_2 \cos \theta, \\ &\quad \theta_1 + \theta_2 \bmod 2\pi), \end{aligned} \quad (2)$$

and the identity is $e = (0, 0, 0)$. The rigid body motion group acts on the homogeneous space of two-dimensional positions and orientations $\mathbb{M}_2 = \mathbb{R}^2 \times S^1 \subseteq \mathbb{R}^2 \times \mathbb{R}^2$ by the left-action \odot :

$$(\mathbf{x}, \mathbf{R}) \odot (\mathbf{y}, \mathbf{n}) = (\mathbf{x} + \mathbf{R}\mathbf{y}, \mathbf{R}\mathbf{n}), \quad (3)$$

with $(\mathbf{x}, \mathbf{R}) \in SE(2)$ and $(\mathbf{y}, \mathbf{n}) \in \mathbb{M}_2$. If context allows it we may omit writing \odot for conciseness. By choosing the reference element $\mathbf{p}_0 = (0, 0, (1, 0)) \in \mathbb{M}_2$ we have:

$$(x, y, \theta) \odot \mathbf{p}_0 = (x, y, (\cos \theta, \sin \theta)). \quad (4)$$

This mapping is a diffeomorphism and allows us to identify $SE(2)$ and \mathbb{M}_2 . Thereby we will also freely use the (x, y, θ) coordinates on \mathbb{M}_2 .

Morphological convolution. Given functions $f_1, f_2 : \mathbb{M}_2 \rightarrow \mathbb{R}$ we define their morphological convolution (or ‘infimal convolution’) [48, 52] by

$$(f_1 \square f_2)(\mathbf{p}) = \inf_{g \in G} \{f_1(g^{-1}\mathbf{p}) + f_2(g\mathbf{p}_0)\} \quad (5)$$

Left-invariant (co-)vector fields on \mathbb{M}_2 . Throughout this paper we shall rely on the following basis of left-invariant vector fields:

$$\begin{aligned} \mathcal{A}_1 &= \cos \theta \partial_x + \sin \theta \partial_y, \\ \mathcal{A}_2 &= -\sin \theta \partial_x + \cos \theta \partial_y, \text{ and} \\ \mathcal{A}_3 &= \partial_\theta. \end{aligned} \quad (6)$$

The dual frame ω^i is given by $\langle \omega^i, \mathcal{A}_j \rangle = \delta_j^i$, i.e:

$$\begin{aligned} \omega^1 &= \cos \theta dx + \sin \theta dy, \\ \omega^2 &= -\sin \theta dx + \cos \theta dy, \text{ and} \\ \omega^3 &= d\theta \end{aligned} \quad (7)$$

Metric tensor fields on \mathbb{M}_2 . We consider the Riemannian left-invariant metric tensor fields:

$$\mathcal{G} = \sum_{i,j=1}^3 g_{ij} \omega^i \otimes \omega^j \quad (8)$$

and write $\|\dot{\mathbf{p}}\| = \sqrt{\mathcal{G}_{\mathbf{p}}(\dot{\mathbf{p}}, \dot{\mathbf{p}})}$. Throughout the paper we restrict our self to the diagonal case and we write $g_{ii} = w_i^2 > 0$. We also use the dual norm $\|\dot{\mathbf{p}}\|_* = \sup_{\dot{\mathbf{p}} \in T_{\mathbf{p}}\mathbb{M}_2} \frac{\langle \dot{\mathbf{p}}, \dot{\mathbf{p}} \rangle}{\|\dot{\mathbf{p}}\|}$. We will assume, without loss of generality, that $w_2 \geq w_1$ and introduce the ratio

$$\zeta := \frac{w_2}{w_1} \geq 1 \quad (9)$$

that is called the *spatial anisotropy* of the metric.

Distances on \mathbb{M}_2 . The left-invariant metric tensor field \mathcal{G} on \mathbb{M}_2 induces a left-invariant distance (‘Riemannian metric’) $d : \mathbb{M}_2 \times \mathbb{M}_2 \rightarrow \mathbb{R}_{\geq 0}$ by

$$d_{\mathcal{G}}(\mathbf{p}, \mathbf{q}) = \inf_{\gamma \in \Gamma_t(\mathbf{p}, \mathbf{q})} \left(L_{\mathcal{G}}(\gamma) := \int_0^t \|\dot{\gamma}(s)\|_{\mathcal{G}} ds \right). \quad (10)$$

where $\Gamma_t(\mathbf{p}, \mathbf{q})$ is the set piecewise C^1 -curves γ in \mathbb{M}_2 with $\gamma(0) = \mathbf{p}$, $\gamma(t) = \mathbf{q}$. The right-hand side does not depend on $t > 0$, and we may set $t = 1$.

If no confusion can arise we omit the subscript \mathcal{G} and write $d, L, \|\cdot\|$ for short. The distance being left-invariant means that for all $g \in SE(2)$, $\mathbf{p}_1, \mathbf{p}_2 \in \mathbb{M}_2$ one has $d(\mathbf{p}, \mathbf{q}) = d(g\mathbf{p}, g\mathbf{q})$. We will often use the shorthand notation $d(\mathbf{p}) := d(\mathbf{p}, \mathbf{p}_0)$.

We often consider the sub-Riemannian case arising when $w_2 \rightarrow \infty$. Then we have ‘infinite cost’ for sideways motion and the only ‘permissible’ curves γ are the ones for which $\dot{\gamma}(t) \in H$ where $H := \text{span}\{\mathcal{A}_1, \mathcal{A}_3\} \subset T\mathbb{M}_2$. This gives rise to a new notion of distance, namely the sub-Riemannian distance d_{sr} :

$$d_{sr}(\mathbf{p}, \mathbf{q}) = \inf_{\substack{\gamma \in \Gamma_t(\mathbf{p}, \mathbf{q}), \\ \dot{\gamma} \in H}} L_{\mathcal{G}}(\gamma). \quad (11)$$

One can show rigorously that when $w_2 \rightarrow \infty$ the Riemannian distance d tends to the sub-Riemannian distance d_{sr} , see for example [27, Thm.2].

Exponential and Logarithm on $SE(2)$. The exponential map $\exp(c^1 \partial x|_e + c^2 \partial y|_e + c^3 \partial \theta|_e) = (x, y, \theta) \in SE(2)$ is given by:

$$\begin{aligned} x &= (c^1 \cos(c^3/2) - c^2 \sin(c^3/2)) \operatorname{sinc}(c^3/2), \\ y &= (c^1 \sin(c^3/2) + c^2 \cos(c^3/2)) \operatorname{sinc}(c^3/2), \\ \theta &= c^3 \bmod 2\pi. \end{aligned} \quad (12)$$

And the logarithm: $\log(x, y, \theta) = c^1 \partial x|_e + c^2 \partial y|_e + c^3 \partial \theta|_e \in T_e SE(2)$:

$$\begin{aligned} c^1 &= \frac{x \cos(\theta/2) + y \sin(\theta/2)}{\operatorname{sinc}(\theta/2)}, \\ c^2 &= \frac{-x \sin(\theta/2) + y \cos(\theta/2)}{\operatorname{sinc}(\theta/2)}, \\ c^3 &= \theta. \end{aligned} \quad (13)$$

By virtue of equation (4) we will freely use the logarithm coordinates on \mathbb{M}_2 .

3 Erosion and Dilation on \mathbb{M}_2

We will be considering the following Hamilton-Jacobi equation on \mathbb{M}_2 :

$$\begin{cases} \frac{\partial W_\alpha}{\partial t} &= \pm \frac{1}{\alpha} \|\nabla W_\alpha\|^\alpha = \pm \mathcal{H}_\alpha(dW_\alpha) \\ W_\alpha|_{t=0} &= U, \end{cases} \quad (14)$$

with the Hamiltonian $\mathcal{H}_\alpha : T^*\mathbb{M}_2 \rightarrow \mathbb{R}_{\geq 0}$:

$$\mathcal{H}_\alpha(\hat{\mathbf{p}}) = \mathcal{H}_\alpha^{1D}(\|\hat{\mathbf{p}}\|) = \frac{1}{\alpha} \|\hat{\mathbf{p}}\|_*^\alpha, \quad (15)$$

and where W_α the viscosity solutions [29] obtained from the initial condition $U \in C(\mathbb{M}_2, \mathbb{R})$. Here the +sign is a dilation scale space and the -sign is an erosion scale space [48, 52]. If no confusion can arise we omit the superscript $1D$. Erosion and dilation correspond to min- and max-pooling, respectively. The Lagrangian $\mathcal{L}_\alpha : T\mathbb{M}_2 \rightarrow \mathbb{R}_{\geq 0}$ corresponding with this Hamiltonian is obtained by taking the Fenchel transform of the Hamiltonian:

$$\mathcal{L}_\alpha(\dot{\mathbf{p}}) = \mathcal{L}_\alpha^{1D}(\|\dot{\mathbf{p}}\|) = \frac{1}{\beta} \|\dot{\mathbf{p}}\|^\beta \quad (16)$$

with β such that $\frac{1}{\alpha} + \frac{1}{\beta} = 1$. Again, if no confusion can arise we omit the subscript α and/or superscript $1D$. We deviate from our previous work by including the factor $\frac{1}{\alpha}$ and working with a power of α instead of 2α . We do this because it simplifies the relation between the Hamiltonian and Lagrangian.

The following proposition collects standard results in terms of the solutions of Hamilton-Jacobi equations on manifolds [1, 21, 30], thereby generalizing results on \mathbb{R}^2 to \mathbb{M}_2 .

Proposition 1 (Solution erosion & dilation)

Let $\alpha > 1$. The viscosity solution W_α of the erosion PDE (14) is given by

$$W_\alpha(\mathbf{p}, t) = \inf_{\substack{\mathbf{q} \in \mathbb{M}_2, \\ \gamma \in \Gamma_t(\mathbf{p}, \mathbf{q})}} U(\mathbf{q}) + \int_0^t \mathcal{L}_\alpha(\dot{\gamma}(s)) \, ds \quad (17)$$

$$= \inf_{\mathbf{q} \in \mathbb{M}_2} U(\mathbf{q}) + t \mathcal{L}_\alpha^{1D}(d(\mathbf{p}, \mathbf{q})/t) \quad (18)$$

$$= (k_t^\alpha \square U)(\mathbf{p}) \quad (19)$$

where the morphological kernel $k_t^\alpha : \mathbb{M}_2 \rightarrow \mathbb{R}_{\geq 0}$ is defined as:

$$k_t^\alpha = t \mathcal{L}_\alpha^{1D}(d/t) = \frac{t}{\beta} \left(\frac{d(\mathbf{p}_0, \cdot)}{t} \right)^\beta. \quad (20)$$

Moreover, the Riemannian distance $d := d(\mathbf{p}_0, \cdot)$ is the viscosity solution of eikonal PDE

$$\|\nabla d\|^2 = \sum_{i=1}^3 (\mathcal{A}_i d/w_i)^2 = 1 \quad (21)$$

with boundary condition $d(\mathbf{p}_0) = 0$. Likewise the viscosity solution of the dilation PDE is

$$W_\alpha(\mathbf{p}, t) = -(k_t^\alpha \square - U)(\mathbf{p}) \quad (22)$$

Proof It is shown by Fathi in [30, Prop.5.3] that (17) is a viscosity solution of the Hamilton-Jacobi equation (14) on a complete connected Riemannian manifold without boundary, under some (weak) conditions on the Hamiltonian and with the initial condition U being Lipschitz. In [21, Thm.2] a similar statement is given but only for compact connected Riemannian manifolds, again under some weak conditions on the Hamiltonian but without any on the initial condition. Next we employ these existing results and provide a self-contained proof of (18) and (19).

Because we are looking at a specific class of Lagrangians, the solutions can be equivalently written as (18). In [21, Prop.2] this form can also be

found. Namely, the Lagrangian \mathcal{L}_α^{1D} is convex for $\alpha > 1$, so for any curve $\gamma \in \Gamma_t := \Gamma_t(\mathbf{p}, \mathbf{q})$ we have by direct application of Jensen's inequality (omitting the superscript $1D$):

$$\mathcal{L}_\alpha \left(\frac{1}{t} \int_0^t \|\dot{\gamma}(s)\| ds \right) \leq \frac{1}{t} \int_0^t \mathcal{L}_\alpha(\|\dot{\gamma}(s)\|) ds, \quad (23)$$

with equality if $\|\dot{\gamma}\|$ is constant. This means that:

$$\inf_{\gamma \in \Gamma_t} t \mathcal{L}_\alpha \left(\frac{L(\gamma)}{t} \right) \leq \inf_{\gamma \in \Gamma_t} \int_0^t \mathcal{L}_\alpha(\|\dot{\gamma}(s)\|) ds, \quad (24)$$

where $L(\gamma) := L_{\mathcal{G}}(\gamma)$, recall (10), is the length of the curve γ . Consider the subset of curves with constant speed $\tilde{\Gamma}_t = \{\gamma \in \Gamma_t \mid \|\dot{\gamma}\| = L(\gamma)/t\} \subset \Gamma_t$. Optimizing over a subset can never decrease the infimum so we have:

$$\inf_{\gamma \in \Gamma_t} \int_0^t \mathcal{L}_\alpha(\|\dot{\gamma}(s)\|) ds \leq \inf_{\gamma \in \tilde{\Gamma}_t} \int_0^t \mathcal{L}_\alpha \left(\frac{L(\gamma)}{t} \right) ds \quad (25)$$

The r.h.s of this equation is equal to the l.h.s of equation (24) as the length of a curve is independent of its parameterization. Thereby we have equality in (24). By monotonicity of \mathcal{L}_α on $\mathbb{R}_{>0}$ we may then conclude that:

$$\begin{aligned} \inf_{\gamma \in \Gamma_t} t \mathcal{L}_\alpha(L(\gamma)/t) &= t \mathcal{L}_\alpha \left(\inf_{\gamma \in \tilde{\Gamma}_t} L(\gamma)/t \right) \\ &= t \mathcal{L}_\alpha(d(\mathbf{p}, \mathbf{q})/t). \end{aligned} \quad (26)$$

That we can write the solution as (19) is a consequence of the left-invariant metric on the manifold. A similar derivation can be found in [50, Thm.30]:

$$\begin{aligned} W_\alpha(\mathbf{p}, t) &= \inf_{\mathbf{q} \in \mathbb{M}_2} U(\mathbf{q}) + t \mathcal{L}_\alpha(d(\mathbf{p}, \mathbf{q})/t) \\ &= \inf_{g \in G} U(g\mathbf{p}_0) + t \mathcal{L}_\alpha(d(\mathbf{p}, g\mathbf{p}_0)/t) \\ &= \inf_{g \in G} U(g\mathbf{p}_0) + t \mathcal{L}_\alpha(d(g^{-1}\mathbf{p}, \mathbf{p}_0)/t) \quad (27) \\ &= \inf_{g \in G} U(g\mathbf{p}_0) + k_t^\alpha(g^{-1}\mathbf{p}) \\ &= (k_t^\alpha \square U)(\mathbf{p}) \end{aligned}$$

It is shown in [1, Thm.6.23] for complete connected Riemannian manifolds that the distance map $d(\mathbf{p})$ is a viscosity solution of the Eikonal equation (21).

Finally, solutions of erosion and dilation PDEs correspond to each other. If W_α is the viscosity solution of the erosion PDE with initial condition U , then $-W_\alpha$ is the viscosity solution of the dilation PDE, with initial condition $-U$. This means that the viscosity solution of the dilation PDE is given by (22). \square

4 Distance Approximations

To calculate the morphological kernel k_t^α (20) we need the the exact Riemannian distance d (10),

but calculating this is computationally demanding. To alleviate this problem we approximate the exact distance $d(\mathbf{p}_0, \cdot)$ with approximative distances, denoted with ρ , which are computationally cheap. To this end we define the logarithmic distance approximation $\rho_c : \mathbb{M}_2 \rightarrow \mathbb{R}_{\geq 0}$, as explained in [50, Def.19], by

$$\rho_c := \sqrt{(w_1 c^1)^2 + (w_2 c^2)^2 + (w_3 c^3)^2}. \quad (28)$$

Note that all approximative distances $\rho : \mathbb{M}^2 \rightarrow \mathbb{R}$ can be extended to something that looks like a metric on \mathbb{M}_2 . For example we can define:

$$\rho(g_1 \mathbf{p}_0, g_2 \mathbf{p}_0) := \rho(g_1^{-1} g_2 \mathbf{p}_0).$$

But this is almost always not a true metric in the sense that it does not satisfy the triangle inequality. So in this sense an approximative distance is not necessarily a true distance. However, we will keep referring to them as approximative distances as we only require them to look like the exact Riemannian distance $d(\mathbf{p}_0, \cdot)$.

As already stated in the introduction, Riemannian distance approximations such as ρ_c begin to fail in the high spatial anisotropy cases $\zeta \gg 1$. For these situations we need sub-Riemannian distance approximations. In previous literature two such sub-Riemannian approximations are suggested. The first one is standard [51, Sec.6], the second one is a modified smooth version [23, p.284], also seen in [6, eq.14]:

$$\sqrt{\sqrt{\nu w_1^2 w_3^2 |c^2|} + (w_1 c^1)^2 + (w_3 c^3)^2} \quad (29)$$

$$\sqrt[4]{\nu w_1^2 w_3^2 |c^2|^2 + ((w_1 c^1)^2 + (w_3 c^3)^2)^2} \quad (30)$$

In [6] $\nu \approx 44$ is empirically suggested. Note that the sub-Riemannian approximations rely on the assumption that $w_2 \geq w_1$.

However, they both suffer from a major shortcoming in the interaction between w_3 and c^2 . When we let $w_3 \rightarrow 0$ both approximations suggest that it becomes arbitrarily cheap to move in the c^2 direction which is undesirable as this deviates from the exact distance d : moving spatially will always have a cost associated with it determined by at least w_1 .

The following sub-Riemannian approximation is more correct in that sense:

$$\rho_{c, sr} := \sqrt[4]{(\nu(w_1 + w_3))^4 |c^2|^2 + ((w_1 c^1)^2 + (w_3 c^3)^2)^2}, \quad (31)$$

again for some ν such that the approximation is appropriate. We empirically suggest $\nu \approx 1.6$. Notice that this approximation does not break down when we let $w_3 \rightarrow 0$. In Section 4.1 a short explanation is given as to how this approximation is derived.

Table 3 shows that both the old sub-Riemannian approximation (30) and new approximation (31) are appropriate in cases such as $w_3 = 1$. Table 4 shows that the old approximation breaks down when we take $w_3 = 0.5$, and that the new approximation behaves more appropriate.

The Riemannian and sub-Riemannian approximations can be combined into the following newly proposed practical approximation:

$$\rho_{c, com} := \max(l, \min(\rho_{c, sr}, \rho_c)), \quad (32)$$

where $l : \mathbb{M}_2 \rightarrow \mathbb{R}$ is given by:

$$l := \sqrt{(w_1 x)^2 + (w_1 y)^2 + (w_3 \theta)^2}, \quad (33)$$

for which will we show that it is a lower bound of the exact distance d in Lemma 4.

The most important property of the combined approximation is that it automatically switches between the Riemannian and sub-Riemannian approximations depending on the metric parameters. Namely, the Riemannian approximation is appropriate very close to the reference point \mathbf{p}_0 , but tends to overestimate the true distance at a moderate distance from it. The sub-Riemannian approximation is appropriate at moderate distances from \mathbf{p}_0 , but tends to overestimate very close to it, and underestimate far away. The combined approximation is such that we get rid of the weaknesses that the approximations have on their own.

On top of these approximative distances, we also define ρ_b , $\rho_{b, sr}$, and $\rho_{b, com}$ by replacing the logarithmic coordinates c^i by their corresponding

half-angle coordinates b^i defined by:

$$\begin{aligned} b^1 &= x \cos(\theta/2) + y \sin(\theta/2), \\ b^2 &= -x \sin(\theta/2) + y \cos(\theta/2), \\ b^3 &= \theta. \end{aligned} \quad (34)$$

So, for example, we define ρ_b as:

$$\rho_b := \sqrt{(w_1 b^1)^2 + (w_2 b^2)^2 + (w_3 b^3)^2}. \quad (35)$$

Why we use these coordinates will be explained in Section 6.1.

We can define approximative morphological kernels by replacing the exact distance in (20) by any of the approximative distances in this section. To this end we, for example, define k_b by replacing the exact distance in the morphological kernel k by ρ_b :

$$k_{b, t}^\alpha := \frac{t}{\beta} \left(\frac{\rho_b}{t} \right)^\beta, \quad (36)$$

where we recall that $\frac{1}{\alpha} + \frac{1}{\beta} = 1$ and $\alpha > 1$.

4.1 Sub-Riemannian Approximation

To make a proper sub-Riemannian distance estimate we will use the Zassenhaus formula, which is related to the Baker–Campbell–Hausdorff formula:

$$e^{t(X+Y)} = e^{tX} e^{tY} e^{-\frac{t^2}{2}[X, Y]} e^{\mathcal{O}(t^3)} \dots, \quad (37)$$

where we have used the shorthand $e^x := \exp(x)$. Filling in $X = A_1$ and $Y = A_3$ and neglecting the higher order terms gives:

$$e^{t(A_1+A_3)} \approx e^{tA_1} e^{tA_3} e^{\frac{t^2}{2}A_2}, \quad (38)$$

or equivalently:

$$e^{\frac{t^2}{2}A_2} \approx e^{-tA_3} e^{-tA_1} e^{t(A_1+A_3)}. \quad (39)$$

This formula says that one can successively follow exponential curves in the “legal” directions A_1 and A_3 to move in the “illegal” direction of A_2 . Taking the lengths of these curves and adding them up gives an approximative upper bound on

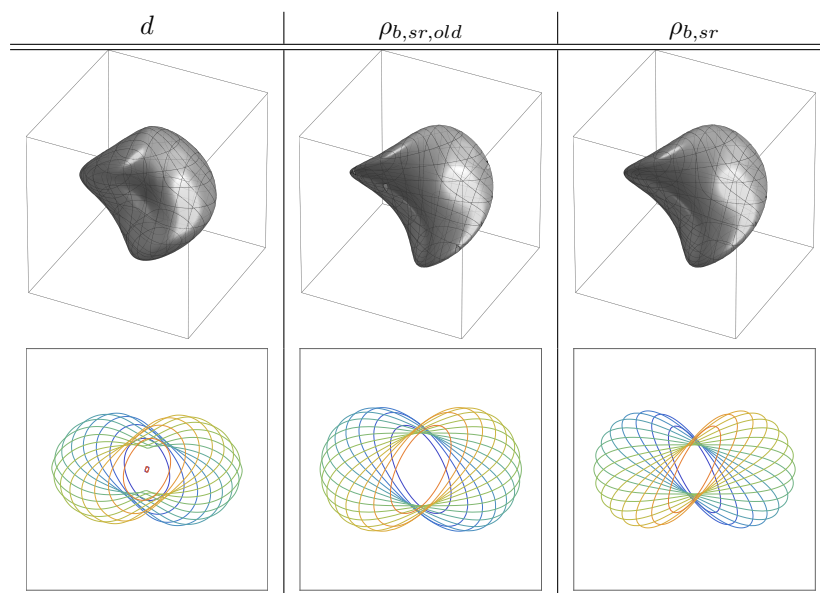


Table 3: Same situation and metric parameters as Table 2, i.e. $w_1 = w_3 = 1$ and $w_2 = 8$. We see the exact distance d alongside the old sub-Riemannian approximation $\rho_{b,sr,old}$ (30) and new approximation $\rho_{b,sr}$ (31). For the old approximation we chose $\nu = 44$, as suggested in [6], and for the new one $\nu = 1.6$. We see that in this case both approximations are appropriate.

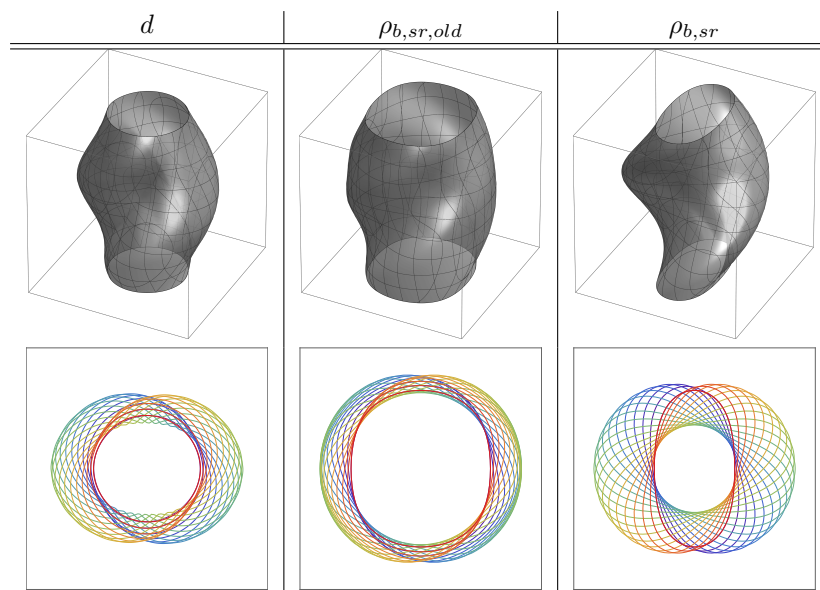


Table 4: Same as Table 3 but then with $w_1 = 1, w_2 = 8, w_3 = 0.5$. We see that in this case that the old sub-Riemannian approximation $\rho_{b,sr,old}$ (30) underestimates the true distance and becomes less appropriate. The new approximation (31) is also not perfect but qualitatively better. Decreasing w_3 would exaggerate this effect even further.

the sub-Riemannian distance:

$$d_{sr}(e^{\frac{t^2}{2}A_2}) \lesssim \left(w_1 + w_3 + \sqrt{w_1^2 + w_3^2} \right) |t| \quad (40)$$

$$\leq 2(w_1 + w_3) |t|.$$

Substituting $t \rightarrow \sqrt{2|t|}$ gives:

$$d_{sr}(e^{tA_2}) \lesssim 2\sqrt{2}(w_1 + w_3) \sqrt{|t|}. \quad (41)$$

This inequality then inspires the following sub-Riemannian distance approximation:

$$\sqrt{(\nu(w_1 + w_3))^2 |c_2| + (w_1 c_1)^2 + (w_3 c_3)^2} \quad (42)$$

for some $0 < \nu < 2\sqrt{2}$ s.t. the approximation is tight. Totally analogous to (29) and (30), we can also modify this approximation to make it more smooth:

$$\rho_{c, sr} = \sqrt[4]{(\nu(w_1 + w_3))^4 |c^2|^2 + ((w_1 c^1)^2 + (w_3 c^3)^2)^2}. \quad (43)$$

Here in view of contraction of $SE(2)$ to the Heisenberg group H_3 [23, Sec.5.2], and the exact fundamental solution [25, Eq.27] of the Laplacian on H_3 (where the norm $\rho_{c, sr}$ appears squared in the numerator with $1 = w_1 = w_3 = \nu$) we expect $\nu \geq 1$.

In our practical experiments we use

$$\rho_{b, sr} = \sqrt[4]{(\nu(w_1 + w_3))^4 |b^2|^2 + ((w_1 b^1)^2 + (w_3 b^3)^2)^2}. \quad (44)$$

where we set $\nu = 1.6$ to get an appropriate approximation, based on a numerical analysis that is tangential to [6, Fig.3].

5 Statement of the Main Theorem

Next we summarize the main theoretical results in the following theorem. As the result applies to all evolution times $t > 0$, we use short notation $k^\alpha := k_t^\alpha, k_b^\alpha := k_{b,t}^\alpha$ because there is no time t dependency in all the inequalities of our main result.

Theorem 1 (Quality of approximative morphological kernels)

Let $\zeta := \frac{w_2}{w_1}$ denote the spatial anisotropy, and let β be

such that $\frac{1}{\alpha} + \frac{1}{\beta} = 1$, for some $\alpha > 1$ fixed. We assess the quality of our approximative kernels in three ways:

- The exact and all approximative kernels have the same symmetries.
- Globally it holds that:

$$\zeta^{-\beta} k^\alpha \leq k_b^\alpha \leq \zeta^\beta k^\alpha, \quad (45)$$

from which we see that in the case $\zeta = 1$ we have that k_b^α is exactly equal to k^α .

- Locally around ¹ \mathbf{p}_0 we have:

$$k_b^\alpha \leq (1 + \varepsilon)^{\beta/2} k^\alpha. \quad (46)$$

where

$$\varepsilon := \frac{\zeta^2 - 1}{2w_3^2} \zeta^4 \rho_b^2 + \mathcal{O}(|\theta|^3). \quad (47)$$

Proof The proof of the parts of the theorem will be discussed throughout the following section.

- The symmetries will be shown in Corollary 1 and is a direct result of Lemma 3.
- The global bound (45) is shown in Corollary 3 and follows from Corollary 2 and Lemma 4.
- The local bound (46) is shown in Corollary 5 and is a direct result of Lemma 7. \square

Clearly, the analysis of the quality of an approximative kernel reduces to analysing the quality of the approximative distance that is used, and this is exactly what we will do in the following section.

6 Analysis

In previous work on PDE-G-CNN's the bound $d = d(\mathbf{p}_0, \cdot) \leq \rho_c$ is proven [50, Lem.20]. Furthermore, it is shown that around \mathbf{p}_0 one has:

$$\rho_c^2 \leq d^2 + \mathcal{O}(d^4), \quad (48)$$

which has the corollary that there exist a constant $C \geq 1$ such that

$$\rho_c \leq Cd \quad (49)$$

¹for a precise statement see Lemma 7 and Remark 3.

for any compact neighbourhood around \mathbf{p}_0 . We improve on these results by;

- Showing that the approximative distances have the same symmetries as the exact Riemannian distance; Lemma 3.
- Finding simple global bounds on the exact distance d which can then be used to find global estimates of ρ_b by d ; Lemma 4. This improves upon (49) by finding an expression for the constant C .
- Estimating the leading term of the asymptotic expansion, and observing that our upper bound of the relative error between ρ_b and d explodes in the cases $\zeta \rightarrow \infty$ and $w_3 \rightarrow 0$; Lemma 7. This improves upon equation (48).

Note however that we are *not* analysing ρ_c : we will be analysing ρ_b . This is mainly because the half-angle coordinates are easier to work with: they do not have the $\text{sinc}(\theta/2)$ factor the logarithmic coordinates have. Using that

$$b^1 = c^1 \text{sinc}(\theta/2), \quad b^2 = c^2 \text{sinc}(\theta/2), \quad b^3 = c^3, \quad (50)$$

recall (34) and (13), we see that

$$\text{sinc}(\theta/2)\rho_c \leq \rho_b \leq \rho_c, \quad (51)$$

and thus locally ρ_c and ρ_b do not differ much, and results on ρ_b can be easily transferred to (slightly weaker) results on ρ_c .

6.1 Symmetry Preservation

Symmetries play a major role in the analysis of (sub-)Riemannian geodesics/distance in $SE(2)$. They help to analyze symmetries in Hamiltonian flows [41] and corresponding symmetries in association field models [22, Fig.11]. There are together 8 of them and their relation with logarithmic coordinates c^i (Lemma 1) shows they correspond to inversion of the Lie-algebra basis $A_i \mapsto -A_i$. The symmetries for the sub-Riemannian setting are explicitly listed on [41, Ch.5, Prop.5.3]. They can be algebraically generated by the (using the same labeling as [41]) following three symmetries:

$$\begin{aligned} \varepsilon^2(x, y, \theta) &= (-x \cos \theta - y \sin \theta, -x \sin \theta + y \cos \theta, \theta), \\ \varepsilon^1(x, y, \theta) &= (x \cos \theta + y \sin \theta, x \sin \theta - y \cos \theta, \theta), \text{ and} \\ \varepsilon^6(x, y, \theta) &= (x \cos \theta + y \sin \theta, -x \sin \theta + y \cos \theta, -\theta). \end{aligned} \quad (52)$$

	ε_0	ε_1	ε_2	ε_3	ε_4	ε_5	ε_6	ε_7
b^1, c^1	+	+	-	-	-	-	+	+
b^2, c^2	+	-	+	-	+	-	+	-
b^3, c^3	+	+	+	+	-	-	-	-

Table 5

They generate the other 4 symmetries as follows:

$$\begin{aligned} \varepsilon^3 &= \varepsilon^2 \circ \varepsilon^1, \quad \varepsilon^4 = \varepsilon^2 \circ \varepsilon^6, \quad \varepsilon^7 = \varepsilon^1 \circ \varepsilon^6, \\ \text{and } \varepsilon^5 &= \varepsilon^2 \circ \varepsilon^1 \circ \varepsilon^6. \end{aligned} \quad (53)$$

and with $\varepsilon^0 = \text{id}$. All symmetries are involutions: $\varepsilon^i \circ \varepsilon^i = \text{id}$. Henceforth all eight symmetries will be called ‘fundamental symmetries’. How all fundamental symmetries relate to each other becomes clearer if we write them down in either logarithm or half-angle coordinates.

Lemma 1 (8 fundamental symmetries)

The 8 fundamental symmetries ε_i in either half-angle coordinates b^i or logarithmic coordinates c^i correspond to sign flips as laid out in Table 5.

Proof We will only show that ε^2 flips b^1 . All other calculations are done analogously.

Pick a point $\mathbf{p} = (x, y, \theta)$ and let $\mathbf{q} = \varepsilon^2(\mathbf{p})$. We now calculate $b^1(\mathbf{q})$:

$$\begin{aligned} b^1(\mathbf{q}) &= x(\mathbf{q}) \cos(\theta(\mathbf{q})/2) + y(\mathbf{q}) \sin(\theta(\mathbf{q})/2) \\ &= -(x \cos \theta + y \sin \theta) \cos(\theta/2) \\ &\quad + (-x \sin \theta + y \cos \theta) \sin(\theta/2) \\ &= -x(\cos \theta \cos(\theta/2) + \sin \theta \sin(\theta/2)) \\ &\quad - y(\sin \cos(\theta/2) - \cos \theta \sin(\theta/2)) \\ &= -x \cos(\theta/2) - y \sin(\theta/2) \\ &= -b^1(\mathbf{p}), \end{aligned} \quad (54)$$

where we have used the trigonometric difference identities of cosine and sine in the second-to-last equality. From the relation between logarithmic and half-angle coordinates (50) we have that the logarithmic coordinates c^i flip in the same manner under the symmetries. \square

The fixed points of the symmetries ε^2 , ε^1 , and ε^6 have an interesting geometric interpretation. The logarithmic and half-angle coordinates, being so closely related to the fundamental symmetries, also carry the same interpretation. Definition 1 introduces this geometric idea and Lemma 2

makes its relation to the fixed points of the symmetries precise. In Figure 12 the fixed points are visualized, and in Figure 13 a visualization of these geometric ideas can be seen.

Definition 1 Two points $\mathbf{p}_1 = (\mathbf{x}_1, \mathbf{n}_1)$, $\mathbf{p}_2 = (\mathbf{x}_2, \mathbf{n}_2)$ of \mathbb{M}_2 are called **cocircular** if there exist a circle, of possibly infinite radius, passing through \mathbf{x}_1 and \mathbf{x}_2 such that the orientations $\mathbf{n}_1 \in S^1$ and $\mathbf{n}_2 \in S^1$ are tangents to the circle, at respectively \mathbf{x}_1 and \mathbf{x}_2 , in either both the clockwise or anti-clockwise direction. Similarly, the points are called **coradial** if the orientations are normal to the circle in either both the outward or inward direction. Finally, two points are called **parallel** if their orientations coincide.

Co-circularity has a well-known characterisation that is often used for line enhancement in image processing, such as tensor voting [35].

Remark 1 Point $\mathbf{p} = (r \cos \phi, r \sin \phi, \theta) \in \mathbb{M}_2$ is cocircular to the reference point $\mathbf{p}_0 = (0, 0, 0)$ if and only if the double angle equality $\theta \equiv 2\phi \pmod{2\pi}$ holds.

In fact all fixed points of the fundamental symmetries can be intuitively characterised:

Lemma 2 (Fixed Points of Symmetries)

Fix reference point $\mathbf{p}_0 = (0, 0, 0) \in \mathbb{M}_2$.

The point $g\mathbf{p}_0 \in \mathbb{M}_2$ with $g \in SE(2)$ is respectively

- cocircular to \mathbf{p}_0 when
$$c^2(g) = 0 \Leftrightarrow \varepsilon_1(g) = g \Leftrightarrow g \in \exp(\langle A_1, A_3 \rangle), \quad (55)$$

- coradial to \mathbf{p}_0 when
$$c^1(g) = 0 \Leftrightarrow \varepsilon_2(g) = g \Leftrightarrow g \in \exp(\langle A_2, A_3 \rangle), \quad (56)$$

- parallel to \mathbf{p}_0 when
$$c^3(g) = 0 \Leftrightarrow \varepsilon_6(g) = g \Leftrightarrow g \in \exp(\langle A_1, A_2 \rangle). \quad (57)$$

Proof We will only show (55), the others are done analogously. We start by writing $g = (r \cos \phi, r \sin \phi, \theta)$ and calculating that $g \odot \mathbf{p}_0 = (r \cos \phi, r \sin \phi, (\cos \theta, \sin \theta))$. Then by Remark 1 we know that $g\mathbf{p}_0$ is cocircular to \mathbf{p}_0 if and only if $2\phi = \theta \pmod{2\pi}$. We can show this is equivalent to $c^2(g) = 0$:

$$\begin{aligned} c^2(g) = 0 &\Leftrightarrow b^2(g) = 0 \\ &\Leftrightarrow -x \sin(\theta/2) + y \cos(\theta/2) = 0 \\ &\Leftrightarrow -\cos(\phi) \sin(\theta/2) + \sin(\phi) \cos(\theta/2) = 0 \\ &\Leftrightarrow \sin(\phi - \theta/2) = 0 \Leftrightarrow 2\phi = \theta \pmod{2\pi}. \end{aligned} \quad (58)$$

In logarithmic coordinates ε_1 is equivalent to:

$$\varepsilon_1(c^1, c^2, c^3) = (c^1, -c^2, c^3) \quad (59)$$

from which we may deduce that $\varepsilon_1(g) = g$ is equivalent to $c^2(g) = 0$. If $c^2(g) = 0$ then $\log g \in \langle A_1, A_3 \rangle$ and thus $g \in \exp(\langle A_1, A_3 \rangle)$. As for the other way around, it holds by simple computation that:

$$c^2(\exp(c^1 A_1 + c^3 A_3)) = 0 \quad (60)$$

which shows that $g \in \exp(\langle A_1, A_3 \rangle) \Rightarrow c^2(g) = 0$. \square

In the important work [41] on sub-Riemannian geometry on $SE(2)$ by Sachkov and Moiseev, it is shown that the exact sub-Riemannian distance d_{sr} is invariant under the fundamental symmetries ε^i . However, these same symmetries hold true for the Riemannian distance d . Moreover, because the approximative distances use the logarithmic coordinates c^i and half-angle coordinates b^i they also carry the same symmetries. The following lemma makes this precise.

Lemma 3 (Symmetries of the exact distance and all proposed approximations)

All exact and approximative (sub)-Riemannian distances (w.r.t. the reference point \mathbf{p}_0) are invariant under all the fundamental symmetries ε_i .

Proof By Table 5 one sees that $\varepsilon^3, \varepsilon^4$, and ε^5 also generate all symmetries. Therefore if we just show that all distances are invariant under these select three symmetries we also have shown that they are invariant under all symmetries. We will first show the exact distance, in either the Riemannian or sub-Riemannian case, is invariant w.r.t these three symmetries, i.e. $d(\mathbf{p}) = d(\varepsilon^i(\mathbf{p}))$ for $i \in \{3, 4, 5\}$.

By (53) and (52) one has $\varepsilon^3(x, y, \theta) = (-x, -y, \theta)$ and $\varepsilon^4(x, y, \theta) = (-x, y, -\theta)$. Now consider the push forward ε_*^3 . By direct computation (in (x, y, θ) coordinates) we have $\varepsilon_*^3 \mathcal{A}_i|_{\mathbf{p}} = \pm \mathcal{A}_i|_{\varepsilon^3(\mathbf{p})}$. Because the metric tensor field \mathcal{G} (8) is diagonal w.r.t to the \mathcal{A}_i basis this means that ε^3 is an isometry. Similarly, ε^4 is an isometry. Being an isometry of the metric \mathcal{G} we may directly deduce that ε^3 and ε^4 preserve distance. The ε^5 symmetry flips all the signs of the c^i coordinates which amounts to Lie algebra inversion: $-\log g = \log(\varepsilon^5(g))$. Taking the exponential on both sides shows that $g^{-1} = \varepsilon^5(g)$. By left-invariance of the metric we have $d(g\mathbf{p}_0, \mathbf{p}_0) = d(\mathbf{p}_0, g^{-1}\mathbf{p}_0)$, which

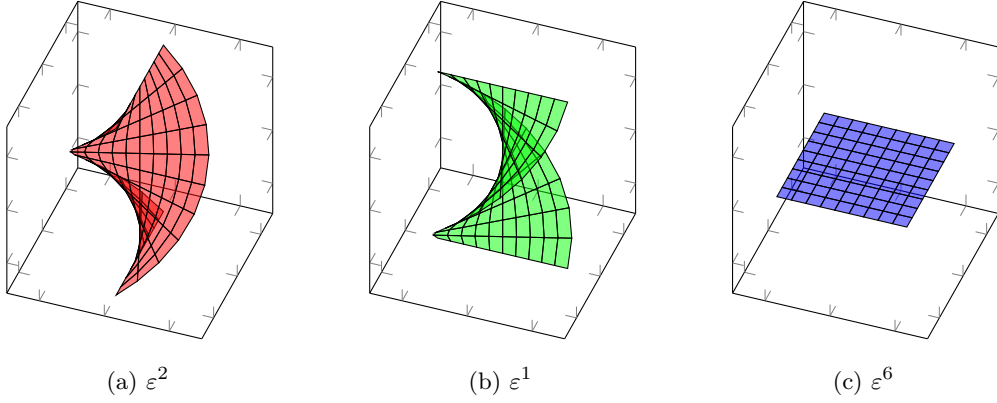


Fig. 12: The fixed points of the ε^2 , ε^1 , and ε^6 . For ε^2 and ε^1 only the points within the region $x^2 + y^2 \leq 2^2$ are plotted. For ε^6 only the points in the region $\max(|x|, |y|) \leq 2$. The fixed points of ε^2 , ε^1 , and ε^6 correspond respectively to the points in \mathbb{M}_2 that are cocircular, coradial, and parallel to the reference point \mathbf{p}_0 .

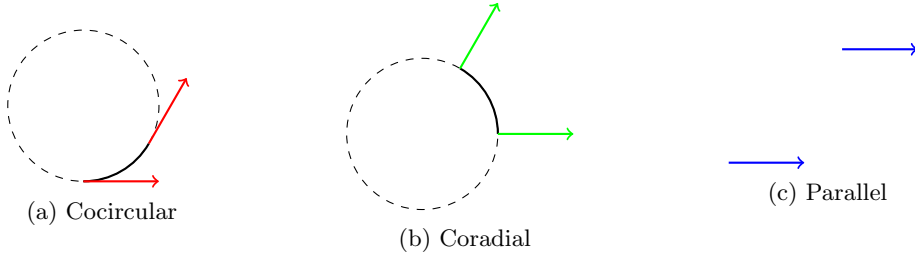


Fig. 13: An example of points in \mathbb{M}_2 that are cocircular, coradial and parallel.

holds in both the Riemannian and sub-Riemannian case, and thus $d(g\mathbf{p}_0) = d(\varepsilon^5(g\mathbf{p}_0))$.

That all approximative distances (both in the Riemannian and sub-Riemannian case) are also invariant under all the symmetries is not hard to see: every b^i and c^i term is either squared or the absolute value is taken. Flipping signs of these coordinates, recall Lemma 1, has no effect on the approximative distance. \square

Corollary 1 (All kernels preserve symmetries)

The exact kernel and all approximative kernels have the same fundamental symmetries.

Proof The kernels are direct functions of the exact and approximative distances, recall for example (20), so from Lemma 3 we can immediately conclude that they also carry the 8 fundamental symmetries. \square

In Figure 10 the previous lemma can be seen. The two fundamental symmetries ε^2 and ε^1 correspond, respectively, to reflecting the isocontours (depicted in colors) along their short edge and long axis. The ε^6 symmetry corresponds to mapping the positive θ isocontours to their negative θ counterparts.

6.2 Simple Global Bounds

Next we provide some basic global lower and upper bounds for the exact Riemannian distance d (10). Recall that the lower bound l plays an important role in the combined approximation $\rho_{c,com}$ (32) when far from the reference point \mathbf{p}_0 .

Lemma 4 (Global bounds on distance)

Let the weights $w_1, w_2, w_3 > 0$ be such that $w_1 \leq w_2$. The exact Riemannian distance $d = d(\mathbf{p}_0, \cdot)$ is greater

than or equal to the following lower bound $l : \mathbb{M}_2 \rightarrow \mathbb{R}$:

$$l := \sqrt{(w_1x)^2 + (w_1y)^2 + (w_3\theta)^2} \leq d \quad (61)$$

and less than or equal to the following upper bounds $u_1, u_2 : \mathbb{M}_2 \rightarrow \mathbb{R}$:

$$d \leq u_1 := \sqrt{(w_2x)^2 + (w_2y)^2 + (w_3\theta)^2} \quad (62)$$

$$d \leq u_2 := \sqrt{(w_1x)^2 + (w_1y)^2} + w_3\pi \quad (63)$$

Proof We will first show $l \leq d$. Consider the following spatially isotropic metric:

$$\tilde{\mathcal{G}} = w_1^2 \omega^1 \otimes \omega^1 + w_1^2 \omega^2 \otimes \omega^2 + w_3^2 \omega^3 \otimes \omega^3. \quad (64)$$

We assumed w.l.o.g. that $w_1 \leq w_2$ so we have for any vector $v \in T\mathbb{M}_2$ that $\|v\|_{\tilde{\mathcal{G}}} \leq \|v\|_{\mathcal{G}}$. From this we can directly deduce that for any curve γ on \mathbb{M}_2 we have that $L_{\tilde{\mathcal{G}}}(\gamma) \leq L_{\mathcal{G}}(\gamma)$. Now consider a length-minimizing curve γ w.r.t \mathcal{G} between the reference point \mathbf{p}_0 and some end point \mathbf{p} . We then have the chain of (in)equalities:

$$d_{\tilde{\mathcal{G}}}(\mathbf{p}) \leq L_{\tilde{\mathcal{G}}}(\gamma) \leq L_{\mathcal{G}}(\gamma) = d_{\mathcal{G}}(\mathbf{p}) \quad (65)$$

Furthermore, because the metric $\tilde{\mathcal{G}}$ is spatially isotropic it can be equivalently be written as:

$$\tilde{\mathcal{G}} = w_1^2 dx \otimes dx + w_1^2 dy \otimes dy + w_3^2 d\theta \otimes d\theta, \quad (66)$$

which is a constant metric on the coordinate covector fields, and thus:

$$d_{\tilde{\mathcal{G}}}(\mathbf{p}) = \sqrt{(w_1x)^2 + (w_1y)^2 + (w_3\theta)^2} = l. \quad (67)$$

Putting everything together gives the desired result of $l \leq d$. To show that $d \leq u_1$ can be done analogously.

As for showing $d \leq u_2$ we will construct a curve γ of which the length $L(\gamma)$ w.r.t. \mathcal{G} can be bounded from above with u_2 . This in turn shows that $d \leq u_2$ by definition of the distance. Pick a destination position and orientation $\mathbf{p} = (\mathbf{x}, \mathbf{n})$. The constructed curve γ will be as follows. We start by aligning our starting orientation $\mathbf{n}_0 = (1, 0) \in S^1$ towards the destination position \mathbf{x} . This desired orientation towards \mathbf{x} is $\hat{\mathbf{x}} := \frac{\mathbf{x}}{r}$ where $r = \|\mathbf{x}\| = \sqrt{x^2 + y^2}$. This action will cost w_3a for some $a \geq 0$. Once we are aligned with $\hat{\mathbf{x}}$ we move towards \mathbf{x} . Because we are aligned this action will cost w_1r . Now that we are at \mathbf{x} we align our orientation with the destination orientation \mathbf{n} , which will cost w_3b for some $b \geq 0$. Altogether we have $L(\gamma) = w_1r + w_3(a + b)$. In its current form the constructed curve actually doesn't have that $a + b \leq \pi$ as desired. To fix this we realise that we did not necessarily had to align with $\hat{\mathbf{x}}$. We could have aligned with $-\hat{\mathbf{x}}$ and move backwards towards \mathbf{x} , which will also cost w_1r . One can show that one of the two methods (either moving forwards or backwards towards \mathbf{x}) indeed has that $a + b \leq \pi$ and thus $d \leq u_2$. \square

These bounds are simple but effective: they help us prove a multitude of insightful corollaries.

Corollary 2 (Global error distance)

Simple manipulations, together with the fact that $x^2 + y^2 = (b^1)^2 + (b^2)^2$, give the following inequalities between l, u_1 and ρ_b :

$$l \leq \rho_b \leq u_1, \quad \frac{1}{\zeta} u_1 \leq \rho_b \leq \zeta l.$$

The second equation can be extended to inequalities between ρ_b and d :

$$\frac{1}{\zeta} d \leq \rho_b \leq \zeta d \quad (68)$$

Remark 2 If $w_1 = w_2 \Leftrightarrow \zeta = 1$, i.e. the spatially isotropic case, then the lower and upper bound coincide, thus becoming exact. Because ρ_b is within the lower and upper bound it also becomes exact.

Corollary 3 (Global error kernel)

Globally the error is independent of time $t > 0$ and is estimated by the spatial anisotropy $\zeta \geq 1$ (9) as follows:

$$\zeta^{-\beta} k^\alpha \leq k_b^\alpha \leq \zeta^\beta k^\alpha. \quad (69)$$

For $\zeta = 1$ there is no error.

Proof We will only prove the second inequality, the first is done analogously.

$$\begin{aligned} k_b^\alpha &:= \frac{1}{\beta} (\rho_b/t)^\beta \leq \frac{1}{\beta} (\zeta d/t)^\beta \\ &= \zeta^\beta \left(\frac{1}{\beta} (d/t)^\beta \right) = \zeta^\beta k^\alpha \end{aligned} \quad (70)$$

\square

The previous result indicates that problems can arise if $\zeta \rightarrow \infty$, which indeed turns out to be the case:

Corollary 4 (Observing the problem)

If we restrict ourselves to $x = \theta = 0$ we have that $u_1 = \rho_b = \rho_c = w_2|y|$. From this we can deduce that one can be certain that both ρ_b and ρ_c become bad approximations away from \mathbf{p}_0 . Namely, when $\zeta > 1 \Leftrightarrow w_2 > w_1$ both approximations go above u_2 if one looks far enough away from \mathbf{p}_0 . How “fast” it goes bad is determined by all metric parameters. Namely, the intersection of the approximations ρ_b and ρ_c , and u_2 is at $|y| = \frac{w_3\pi}{w_2 - w_1}$, or equivalently at $\rho = \frac{w_3\pi}{1 - \zeta - 1}$. This intersection is visible in Figure 14 in the higher

anisotropy cases. From this expression of the intersection we see that in the cases $w_3 \rightarrow 0$ and $\zeta \rightarrow \infty$ the Riemannian distance approximations ρ_b and ρ_c quickly go bad. We will see exactly the same behaviour in Lemma 7 and Remark 3.

Lemma 4 is visualized in Figures 14 and 15. In Figure 14 figure we consider the behavior of the exact distance and bounds along the y -axis, that is at $x = \theta = 0$. We have chosen to inspect the y -axis because it consist of points that are hard to reach from the reference point \mathbf{p}_0 when the spatial anisotropy is large, which makes it interesting. In contrast, along the x -axis $l, d, \rho_b, \rho_c, u_1$ and $w_1 |x|$ all coincide, and is therefor uninteresting. To provide more insight we also depict the bounds along the $y = x$ axis, see Figure 15. Observe that in both figures, the exact distance d is indeed always above the lower bound l and below the upper bounds u_1 and u_2 .

6.3 Asymptotic Error Expansion

In this section we provide an asymptotic expansion of the error between the exact distance d and the half-angle distance approximation ρ_b (Lemma 7). This error is then leveraged to an error between the exact morphological kernel k and the half-angle kernel k_b (Corollary 5). We also give a formula that determines a region for which the half-angle approximation ρ_b is appropriate given an a priori tolerance bound (Remark 3).

Lemma 5 *Let $\gamma : [0, 1] \rightarrow \mathbb{M}_2$ be a minimizing geodesic from \mathbf{p}_0 to \mathbf{p} . We have that:*

$$\rho_b(\mathbf{p}) \leq d(\mathbf{p}) \max_{t \in [0, 1]} \|d\rho_b|_{\gamma(t)}\|. \quad (71)$$

Proof The fundamental theorem of calculus tells us that:

$$\int_0^1 (\rho_b \circ \gamma)'(t) dt = \rho_b(\gamma(1)) - \rho_b(\gamma(0)) = \rho_b(\mathbf{p}), \quad (72)$$

but one can also bound this expression as follows:

$$\int_0^1 (\rho_b \circ \gamma)'(t) dt = \int_0^1 \langle d\rho_b|_{\gamma(t)}, \dot{\gamma}(t) \rangle dt \quad (73)$$

$$\leq \int_0^1 \|d\rho_b|_{\gamma(t)}\| \|\dot{\gamma}(t)\| dt \quad (74)$$

$$\leq \left(\max_{t \in [0, 1]} \|d\rho_b|_{\gamma(t)}\| \right) \int_0^1 \|\dot{\gamma}(t)\| dt \quad (75)$$

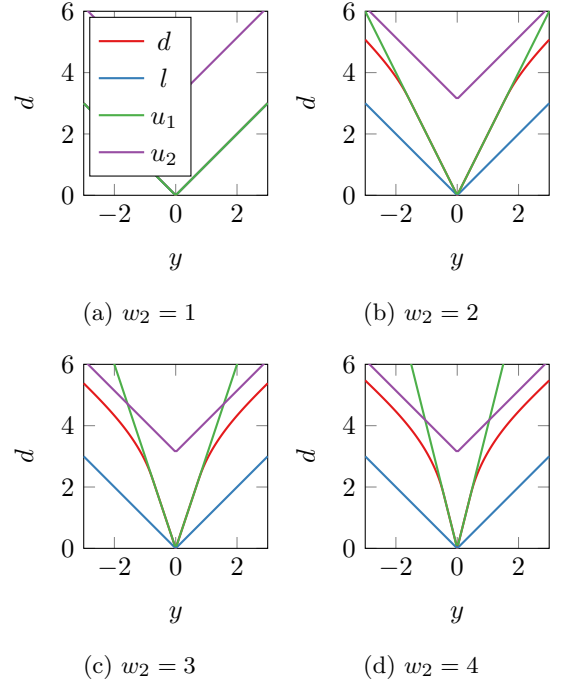


Fig. 14: Exact distance and its lower and upper bounds (given in Lemma 4) along the y -axis, i.e at $x = \theta = 0$, for increasing spatial anisotropy. We keep $w_1 = w_3 = 1$ and vary w_2 . The horizontal axis is y and the vertical axis the value of the distance/bound. Note how the exact distance d starts of linearly with a slope of w_2 , and ends linearly with a slope of w_1 .

$$= d(\mathbf{p}) \max_{t \in [0, 1]} \|d\rho_b|_{\gamma(t)}\|. \quad (76)$$

Putting the two together gives the desired result. \square

Lemma 6 *One can bound $\|d\rho_b\|$ around \mathbf{p}_0 by:*

$$\|d\rho_b\|^2 \leq 1 + \frac{\zeta^2 - 1}{2w_3^2} \rho_b^2 + \mathcal{O}(\theta^3). \quad (77)$$

Proof The proof is deferred to Appendix A \square

By combining the simple Lemmas 5 and 6 one can find an expression for the asymptotic error between the exact distance d and the half-angle approximation ρ_b .

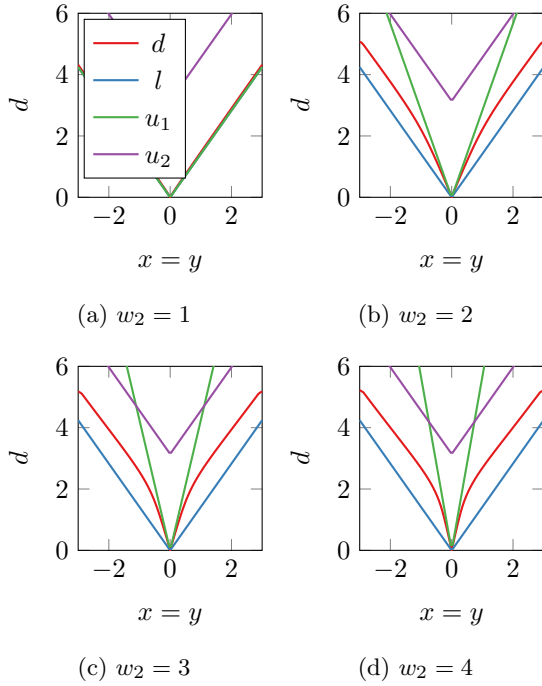


Fig. 15: Same settings as Figure 14 but at $x = y, \theta = 0$. The horizontal axis moves along the line $x = y$.

Lemma 7 *Around any compact neighbourhood of \mathbf{p}_0 we have that*

$$\rho_b^2 \leq d^2(1+\varepsilon), \text{ where } \varepsilon := \frac{\zeta^2 - 1}{2w_3^2} \zeta^4 \rho_b^2 + C|\theta|^3. \quad (78)$$

for some $C \geq 0$.

Proof Let $\mathbf{p} \in U$ be given, and let $\gamma : [0, 1] \rightarrow \mathbb{M}_2$ be the geodesic from \mathbf{p}_0 to \mathbf{p} . For the distance we know that

$$d(\gamma(s)) \leq d(\gamma(t)), \text{ for } s \leq t. \quad (79)$$

Making use of (68) we know that $\frac{1}{\zeta}\rho_b \leq d \leq \zeta\rho_b$ so we can combine this with the previous equation to find:

$$\rho_b(\gamma(s)) \leq \zeta^2 \rho_b(\gamma(t)), \text{ for } s \leq t. \quad (80)$$

from which we get that

$$\max_{t \in [0, 1]} \rho_b(\gamma(t)) \leq \zeta^2 \rho_b(\mathbf{p}). \quad (81)$$

Combining this fact with the above two lemmas allows us to conclude (78). \square

Remark 3 (Region for approximation $\rho_b \approx d$)

Putting an *a priori* tolerance bound ε_{tol} on the error ε

(and neglecting the $\mathcal{O}(\theta^3)$ term) gives rise to a region Ω_0 on which the local approximation ρ_b is appropriate:

$$\Omega_0 = \{\mathbf{p} \in \mathbb{M}_2 \mid \rho_b(\mathbf{p}) < \frac{2w_3^2}{(\zeta^2 - 1)\zeta^4} \varepsilon_{tol}\}. \quad (82)$$

Thereby we can not guarantee a large region of acceptable relative error when $w_3 \rightarrow 0$ or $\zeta \rightarrow \infty$. We solve this problem by using $\rho_{b,com}$ given (32) instead of ρ_b .

Corollary 5 (Local error morphological kernel)

Locally around \mathbf{p}_0 within Ω_0 we have:

$$k_b^\alpha < (1 + \varepsilon_{tol})^{\beta/2} k^\alpha. \quad (83)$$

Proof By Lemma 7 one has

$$k_b^\alpha := \frac{1}{\beta} (\rho_b/t)^\beta \leq \frac{1}{\beta} (d^2(1+\varepsilon)/t^2)^{\beta/2} = (1+\varepsilon)^{\beta/2} k^\alpha$$

Then by Remark 3 we set $\varepsilon = \varepsilon_{tol}$ take $\mathbf{p}_0 \in \Omega_0$ close enough to the origin so that the $\mathcal{O}(\theta^3)$ term indeed becomes negligible. \square

Remark 4 (Linear error on the kernel)

By application of Newton's binomial theorem we can rewrite Corollary 5 as

$$k_b^\alpha \leq (1 + \varepsilon_{tol}\beta/2) k^\alpha + \mathcal{O}(\varepsilon_{tol}^2) \quad (84)$$

from which we see that the leading term of the relative error between the approximative kernel k_b^α and the exact kernel k^α is linear in ε , which means in turn that it is quadratic in the approximative distance ρ_b .

Remark 5 (Alternative to Lemma 7)

Another reasonable strategy to arrive at a similar result is by Taylor expansion of the metric tensor field parameters expressed in half-angle coordinates b^i . This approach gives the following upper bound on a slightly different relative error:

$$\rho_b^2(1 - \varepsilon) \leq d^2, \text{ where } \varepsilon = \frac{\rho_b^2}{6} \frac{4\zeta^2 - 3}{w_3^2} + \mathcal{O}(\rho_b^3). \quad (85)$$

In [11, Sec.4.3] this more technical approach is worked out. Note that for $\zeta \rightarrow 1$ approximation (85) is much less accurate than our result in (78). However, for $\zeta \gg 1$ estimate (85) turns out to be sharper than (78). A detailed analysis and comparison of the estimates is left for future work.

7 Experiments

7.1 Error of Half Angle Approximation

We can quantitatively analyse the error between any distance approximation ρ and the exact

Riemannian distance d as follows. We do this by first choosing a region $\Omega \subseteq \mathbb{M}_2$ in which we will analyse the approximation. Just as in Tables 1 and 2 we decided to inspect $\Omega := [-3, 3] \times [-3, 3] \times [-\pi, \pi] \subseteq \mathbb{M}_2$. As for our exact measure of error ε we have decided on the *mean relative error* defined as:

$$\varepsilon := \frac{1}{\mu(\Omega)} \int_{\Omega} \frac{|\rho_b(\mathbf{p}) - d(\mathbf{p})|}{d(\mathbf{p})} d\mu(\mathbf{p}) \quad (86)$$

where μ is the induced Riemannian measure determined by the Riemannian metric \mathcal{G} . We then discretized our domain Ω into a grid of $101 \times 101 \times 101$ equally spaced points $\mathbf{p}_i \in \Omega$ indexed by some index set $i \in I$ and numerically solved for the exact distance d on this grid. This numerical scheme is of course not exact and we will refer to these values as $\tilde{d}_i \approx d(\mathbf{p}_i)$. We also calculate the value of the distance approximation ρ on the grid points $\rho_i := \rho(\mathbf{p}_i)$. Once we have these values we can approximate the true mean relative error ε by calculating the numerical error $\tilde{\varepsilon}$ defined by:

$$\varepsilon \approx \tilde{\varepsilon} := \frac{1}{|I|} \sum_{i \in I} \frac{|\rho_i - \tilde{d}_i|}{\tilde{d}_i} \quad (87)$$

In Table 6 the numerical mean relative error $\tilde{\varepsilon}$ between the half-angle approximation ρ_b and the numerical Riemannian distance \tilde{d} can be seen for different spatial anisotropies ζ . We keep $w_1 = w_3 = 1$ constant and vary w_2 . We see that, as shown visually in Tables 1 and 2, that ρ_b gets worse and worse when we increase the spatial anisotropy ζ .

There is an discrepancy in the table worth mentioning. We know from Remark 2 that when $\zeta = 1$ then $\rho_b = d$ and thus $\varepsilon = 0$. But surprisingly we do not have $\tilde{\varepsilon} = 0$ in the $\zeta = 1$ case in Table 6. This can be simply explained by the fact that the numerical solution \tilde{d} is not exactly equal to the true distance d . We expect that $\tilde{\varepsilon}$ will go to 0 in the $\zeta = 1$ case if we discretize our region Ω more and more finely.

We can compare these numerical results to our theoretical results. Namely, we can deduce from

ζ	1	1.5	2	3	4	6	8
$\tilde{\varepsilon}$	0.027	0.051	0.14	0.41	0.71	1.4	2.1

Table 6: Numerical mean relative error $\tilde{\varepsilon}$ between ρ_b and d for multiple spatial anisotropies ζ .

Equation (68) that:

$$\frac{|\rho_b - d|}{d} \leq \zeta - 1, \quad (88)$$

which means

$$\varepsilon \leq \zeta - 1. \quad (89)$$

And so we expect this to also approximately hold for the numerical mean relative error $\tilde{\varepsilon}$. Indeed, in Table 6 we can see that $\tilde{\varepsilon} \lesssim \zeta - 1$.

Interestingly, we see that $\tilde{\varepsilon}$ is relatively small compared to our theoretical bound (89) even in the high anisotropy cases. However, this is only a consequence of relative smallness of Ω . If we make Ω bigger and bigger we can be certain that ε converges to $\zeta - 1$. This follows from an argument similar to the reasoning in Corollary 4.

7.2 DCA1

We have split the DCA1 dataset [14] into a training and test set consisting of 125 and 10 images respectively. To establish a baseline we ran a 3, 6, and 12 layer CNN, G-CNN and PDE-G-CNN on DCA1. For the baseline the ρ_c distance approximation was used within the PDE-G-CNNs. Every network was trained 10 times for 80 epochs. After every epoch the average Dice coefficient on the test set is stored. After every full training the maximum of the average Dice coefficients over all 80 epochs is calculated. The result is 10 maximum average Dice coefficients for every architecture. The result of this baseline can be seen in Figure 16. The amount of parameters of the networks can be found in Table 7. We see that PDE-G-CNNs consistently perform equally well as, and sometimes outperform, G-CNNs and CNNs, all the while having the least amount of parameters of all architectures.

To compare the effect of using different approximative distances we decided to train the 6 layer PDE-G-CNN (with 2560 parameters) 10 times for 80 epochs using each corresponding distance approximation. The results can be found in Figure 17. We see that on the DCA1 dataset all

Parameters	3 layers	6 layers	12 layers
CNN	2814	25662	73614
G-CNN	2058	24632	72728
PDE-G-CNN	1264	2560	2698

Table 7: The total amount of parameters in the networks that are used in Figure 16.

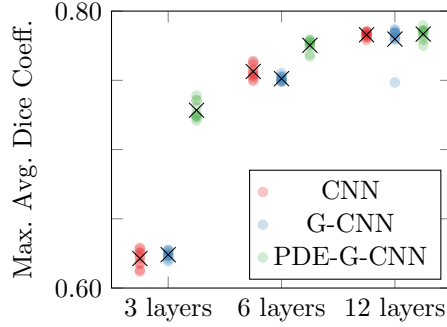


Fig. 16: A scatterplot showing how a 3, 6, and 12 layer CNN, G-CNN, and PDE-G-CNN compare on the DCA1 dataset. The crosses indicate the mean. We see the PDE-G-CNNs provide equal or better results with respectively 2, 10 and 35 times less parameters, see Table 7.

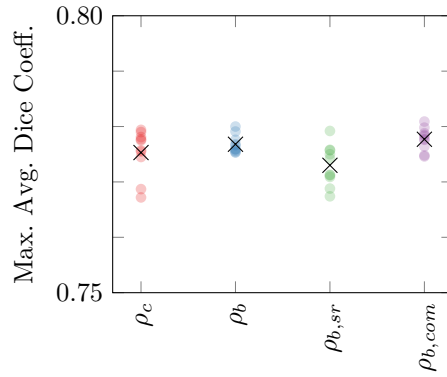


Fig. 17: A scatterplot showing how the use of different distance approximations effect the performance of the 6 layer PDE-G-CNN on the DCA1 dataset. The crosses indicate the mean.

distance approximations have a comparable performance. We notice a small dent in effectiveness when using $\rho_{b,sr}$, and a small increase when using $\rho_{b,com}$.

	CNN	G-CNN	PDE-G-CNN
Parameters	25662	24632	6018

Table 8: The total amount of parameters in the networks that are used in Figure 18.

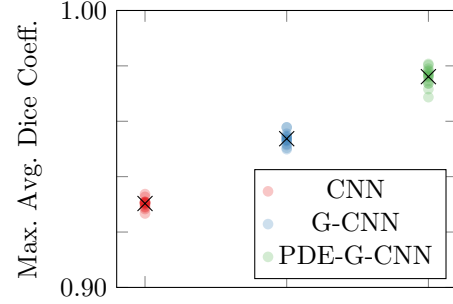


Fig. 18: A scatterplot showing how a 6 layer CNN, G-CNN (both with $\approx 25k$ parameters), and a PDE-G-CNN (with only 6k parameters) compare on the Lines dataset. The crosses indicate the mean. For the precise amount of parameters see Table 8.

7.3 Lines

For the line completion problem we created a dataset of 512 training images and 128 test images. To establish a baseline we ran a 6 layer CNN, G-CNN and PDE-G-CNN. For this baseline we again used ρ_c within the the PDE-G-CNN, but changed the amount of channels to 30, and the kernel sizes to $[9, 9, 9]$, making the total amount of parameters 6018. By increasing the kernel size we anticipate that the difference in effectiveness of using the different distance approximations, if there is any, becomes more pronounced. Every network was trained 15 times for 60 epochs. The result of this baseline can be seen in Figure 18. The amount of parameters of the networks can be found in Table 8. We again see that the PDE-G-CNN outperforms the G-CNN, which in turn outperforms the CNN, while having the least amount of parameters.

We again test the effect of using different approximative distances by training the 6 layer PDE-G-CNN 15 times for 60 epochs for every approximation. The results can be found in Figure 19. We see that on the Lines dataset all distance approximations again have a comparable performance. We again notice an increase

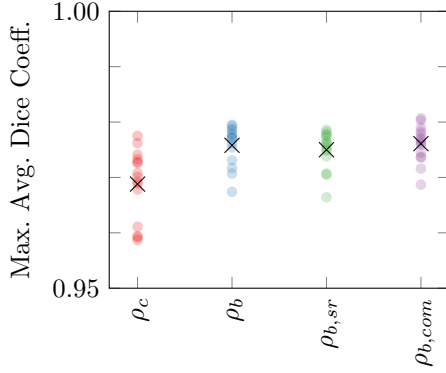


Fig. 19: A scatterplot showing how the use of different distance approximations effect the performance of the 6 layer PDE-G-CNN on the Lines dataset. The crosses indicate the mean.

in effectiveness when using $\rho_{b,com}$, just as on the DCA1 dataset. Interestingly, using $\rho_{b,sr}$ does not seem to hurt the performance on the Lines dataset, which is in contrast with DCA1. This is in line with what one would expect in view of the existing sub-Riemannian line-perception models in neurogeometry.

8 Conclusion

In this article we have carefully analyzed how well the non-linear part of PDE-G-CNNs in previous works actually solves the nonlinear erosion and dilation on the homogeneous space of 2D positions and orientations \mathbb{M}_2 . According to Proposition 1 the Hamilton-Jacobi equations are solved by morphological kernels that are functions of only the exact (sub)-Riemannian distance function. As a result, every approximation of the exact distance yields a corresponding approximative morphological kernel.

In Theorem 1 we use this to improve upon local and global approximations of the relative errors of the erosion and dilations kernels used in the papers [45, 50] where PDE-G-CNN are first proposed (and shown to outperform G-CNNs). Our new sharper estimates for distance on \mathbb{M}_2 have bounds that explicitly depend on the metric tensor field coefficients. This allowed us to theoretically underpin the earlier worries expressed in [50, Fig.10] that if spatial anisotropy becomes high the previous morphological kernel approximations [50] become less and less accurate.

Indeed, as we show in qualitatively in Table 2 and quantitatively in Section 7.1, if the spatial anisotropy ζ is high one must resort to the use of sub-Riemannian approximations. Furthermore, we propose a single distance approximation $\rho_{b,com}$ that works both for low and high spatial anisotropy.

Apart from how well the kernels approximate the PDEs, there is the issue of how well each of the distance approximations perform in applications within the PDE-G-CNNs. In practice the analytic approximative kernels using ρ_b , ρ_c , $\rho_{b,com}$ perform similarly. This is not surprising as our theoretical result Lemma 3 and corollary 1 reveals that all morphological kernel approximations carry the correct 8 fundamental symmetries of the PDE. Nevertheless, Figures 17 and 19 do reveal advantages of using the new kernel approximations (in particular $\rho_{b,com}$) over the previous kernel ρ_c in [50].

The experiments also show that the strictly sub-Riemannian distance approximation $\rho_{b,sr}$ only performs well on applications where sub-Riemannian geometry really applies. For instance, as can be seen in Figures 17 and 19, on the DCA1 dataset $\rho_{b,sr}$ performs relatively poor, whereas on the Lines dataset, $\rho_{b,sr}$ performs well. This is what one would expect in view of sub-Riemannian models and findings in cortical line-perception [2, 3, 15, 33, 44] in neurogeometry.

Besides better accuracy and better performance of the approximative kernels, there is the issue of geometric interpretability. In G-CNNs and CNNs geometric interpretability is absent, as they include ad-hoc nonlinearities like ReLUs. PDE-G-CNNs instead employ morphological convolutions with kernels that reflect association fields, as visualized in Figure 5b. In Figure 8 we see that as network depth increases association fields visually merge in the feature maps of PDE-G-CNNs towards adaptive line detectors, whereas such merging/grouping of association fields is not visible in normal CNNs.

In all cases, the PDE-G-CNNs still outperform G-CNNs and CNNs on the DCA1 dataset and Lines dataset: they have a higher (or equal) performance, while having a huge reduction in network complexity, even when using 3 layers. Regardless, the choice of kernel ρ_c , ρ_b , $\rho_{b,sr}$, $\rho_{b,com}$ the advantage of PDE-G-CNNs towards G-CNNs and CNNs is significant, as can be clearly observed in

Figures 16 and 18 and tables 7 and 8. This is in line with previous observations on other datasets [50].

Altogether, PDE-G-CNNs have a better geometric reduction, performance, and geometric interpretation, than basic classical feed-forward (G)-CNN networks on various segmentation problems.

Extensive investigations on training data reduction, memory reduction (via U-Net versions of PDE-G-CNNs), and the topological description of merging association fields are beyond the scope of this article, and are left for future work.

Acknowledgements

We gratefully acknowledge the Dutch Foundation of Science NWO for financial support (Duits, Geometric learning for Image Analysis, VI.C 202–031). We thank Dr. Xavier Olivan Bescos for pointing us to the publicly available DCA1 dataset.

Appendix A Proof of Lemma 6

Proof We start by writing out the explicit form of $\|d\rho_b\|^2$, which is given by

$$\begin{aligned} & w_2^{-2} \left(\left| \frac{\partial \rho}{\partial b^1} \right|^2 + \left| \frac{\partial \rho}{\partial b^2} \right|^2 \right) \\ & + (w_1^{-2} - w_2^{-2}) \left| \cos \left(\frac{b^3}{2} \right) \frac{\partial \rho}{\partial b^1} + \sin \left(\frac{b^3}{2} \right) \frac{\partial \rho}{\partial b^2} \right|^2 \\ & + w_3^{-2} \left| \frac{1}{2} \frac{\partial \rho}{\partial \psi} + \frac{\partial \rho}{\partial b^3} \right|^2. \end{aligned} \quad (\text{A1})$$

Where we omitted the subscript b from ρ for conciseness. We are going to Taylor expand the sin and cosine in the second term up to the second order term. This becomes

$$\begin{aligned} & \left| \cos \left(\frac{b^3}{2} \right) \frac{\partial \rho}{\partial b^1} + \sin \left(\frac{b^3}{2} \right) \frac{\partial \rho}{\partial b^2} \right|^2 = \left| \frac{\partial \rho}{\partial b^1} \right|^2 \\ & + \theta \left(\frac{\partial \rho}{\partial b^1} \frac{\partial \rho}{\partial b^2} \right) + \frac{\theta^2}{4} \left(\left| \frac{\partial \rho}{\partial b^2} \right|^2 - \left| \frac{\partial \rho}{\partial b^1} \right|^2 \right) + O(\theta^3). \end{aligned} \quad (\text{A2})$$

This allows us to write $\|d\rho_b\|^2$ as

$$w_1^{-2} \left| \frac{\partial \rho}{\partial b^1} \right|^2 + w_2^{-2} \left| \frac{\partial \rho}{\partial b^2} \right|^2 + w_3^{-2} \left| \frac{\partial \rho}{\partial b^3} \right|^2 + \varepsilon. \quad (\text{A3})$$

Making use of the fact that the first part in this expression equals 1, we can thus write $\|d\rho_b\|^2 = 1 + \varepsilon$. The exact form of ε is as follows

$$\begin{aligned} \varepsilon = & \frac{w_1^2 - w_2^2}{4w_1^2 w_2^2 w_3^2 \rho_b^2} \left(w_1^4 w_3^2 (b^1 b^3)^2 - w_2^4 w_3^2 (b^2 b^3)^2 \right. \\ & \left. + w_1^2 w_2^2 (w_1^2 - w_2^2) (b^1 b^2)^2 \right) + O(\theta^3). \end{aligned} \quad (\text{A4})$$

Using that $w_i |b^i| \leq \rho_b$ we can bound the expression from above by

$$\varepsilon \leq \rho_b^2 \frac{|w_1^2 - w_2^2|}{4w_1^2 w_2^2 w_3^2} \left(w_1^2 + w_2^2 + |w_1^2 - w_2^2| \right) + O(\theta^3). \quad (\text{A5})$$

Finally the lemma follows by algebraic manipulations and the fact that $w_1 \leq w_2$. \square

References

- [1] Daniel Azagra, Juan Ferrera, and Fernando Lopez-Mesas. Nonsmooth analysis and Hamilton-Jacobi equations on Riemannian manifolds, 2003.
- [2] Emre Baspinar, Luca Calatroni, Valentina Franceschi, and Dario Prandi. A cortical-inspired sub-Riemannian model for Poggendorff-type visual illusions. *Journal of Imaging*, 7:41, 02 2021.
- [3] Emre Baspinar, Giovanna Citti, and Alessandro Sarti. A geometric model of multi-scale orientation preference maps via Gabor functions. *Journal of Mathematical Imaging and Vision*, 60(6):900–912, 2018.
- [4] E.J. Bekker. *Retinal Image Analysis using Sub-Riemannian Geometry in SE(2)*. PhD thesis, Eindhoven University of Technology, 2017.
- [5] Erik J. Bekkers. B-Spline CNNs on Lie groups. *CoRR*, abs/1909.12057, 2019.
- [6] Erik J. Bekkers, Da Chen, and Jorg M. Portegies. Nilpotent approximations of sub-Riemannian distances for fast perceptual grouping of blood vessels in 2D and 3D. *Journal of Mathematical Imaging and Vision*, 60(6):882–899, Jul 2018.

- [7] Erik J Bekkers, Remco Duits, Alexey Mashnikov, and Gonzalo R Sanguinetti. A PDE approach to data-driven sub-Riemannian geodesics in $SE(2)$. *SIAM Journal on Imaging Sciences*, 8(4):2740–2770, 2015.
- [8] Erik J Bekkers, Maxime W Lafarge, Mitko Veta, Koen AJ Eppenhof, Josien PW Pluim, and Remco Duits. Roto-translation covariant convolutional networks for medical image analysis. In *International Conference on Medical Image Computing and Computer-Assisted Intervention*, pages 440–448. Springer, 2018.
- [9] Erik Johannes Bekkers, Marco Loog, Bart M. ter Haar Romeny, and Remco Duits. Template matching via densities on the roto-translation group. *IEEE Transactions on Pattern Analysis and Machine Intelligence*, 40(2):452–466, 2018.
- [10] Alexander Bogatskiy, Brandon Anderson, Jan T. Offermann, Marwah Roussi, David W. Miller, and Risi Kondor. Lorentz group equivariant neural network for particle physics, 2020.
- [11] D. Bon. *Analysis and Geometric Interpretation of PDE-G-CNNs*. Master thesis, Eindhoven University of Technology, 2022.
- [12] W. H. Bosking, Y. Zhang, B. Schofield, and D. Fitzpatrick. Orientation selectivity and the arrangement of horizontal connections in tree shrew striate cortex. *The Journal of Neuroscience*, 17(6):2112–2127, March 1997.
- [13] Michael M. Bronstein, Joan Bruna, Taco Cohen, and Petar Veličković. Geometric deep learning: Grids, groups, graphs, geodesics, and gauges, 2021.
- [14] Fernando Cervantes-Sanchez, Ivan Cruz-Aceves, Arturo Hernandez-Aguirre, Martha Alicia Hernandez-Gonzalez, and Sergio Eduardo Solorio-Meza. Automatic segmentation of coronary arteries in x-ray angiograms using multiscale analysis and artificial neural networks. *Applied Sciences*, 9(24), 2019.
- [15] G. Citti and A. Sarti. A cortical based model of perceptual completion in the roto-translation space. *Journal of Mathematical Imaging and Vision*, 24(3):307–326, 2006.
- [16] Taco Cohen, Maurice Weiler, Berkay Kicanaoglu, and Max Welling. Gauge equivariant convolutional networks and the icosahedral CNN. In Kamalika Chaudhuri and Ruslan Salakhutdinov, editors, *Proceedings of the 36th International Conference on Machine Learning*, volume 97 of *Proceedings of Machine Learning Research*, pages 1321–1330. PMLR, 09–15 Jun 2019.
- [17] Taco S Cohen, Mario Geiger, and Maurice Weiler. A general theory of equivariant CNNs on homogeneous spaces. *Advances in Neural Information Processing Systems*, 32, 2019.
- [18] T.S. Cohen and M. Welling. Group equivariant convolutional networks. *Proc. of the 33rd Int. Conf. on Machine Learning*, 48:1–12, 2016.
- [19] Sander Dieleman, Jeffrey De Fauw, and Koray Kavukcuoglu. Exploiting cyclic symmetry in convolutional neural networks. *arXiv preprint arXiv:1602.02660*, 2016.
- [20] Sander Dieleman, Kyle W Willett, and Joni Dambre. Rotation-invariant convolutional neural networks for galaxy morphology prediction. *Monthly Notices of the Royal Astronomical Society*, 450(2):1441–1459, 2015.
- [21] El Hadji S Diop, Alioune Mbengue, Bakary Manga, and Diaraf Seck. Extension of mathematical morphology in Riemannian spaces. In *International Conference on Scale Space and Variational Methods in Computer Vision*, pages 100–111. Springer, 2021.
- [22] R. Duits, U. Boscaín, F. Rossi, and Y. Sachkov. Association fields via cusplless sub-Riemannian geodesics in $SE(2)$. *Journal of Mathematical Imaging and Vision*, 49(2):384–417, 2014.
- [23] R. Duits and E. M. Franken. Left invariant parabolic evolution equations on $SE(2)$

and contour enhancement via invertible orientation scores, part I: Linear left-invariant diffusion equations on $SE(2)$. *QAM-AMS*, 68:255–292, 2010.

- [24] Remco Duits. *Perceptual organization in image analysis: a mathematical approach based on scale, orientation and curvature*. PhD thesis, Eindhoven University of Technology, 2005.
- [25] Remco Duits and Bernhard Burgeth. Scale spaces on Lie groups. In *International Conference on Scale Space and Variational Methods in Computer Vision*, pages 300–312. Springer, 2007.
- [26] Remco Duits, Tom Dela Haije, Eric Creusen, and Arpan Ghosh. Morphological and linear scale spaces for fiber enhancement in dw-mri. *Journal of Mathematical Imaging and Vision*, 46(3):326–368, 2013.
- [27] Remco Duits, Stephan PL Meesters, J-M Mirebeau, and Jorg M Portegies. Optimal paths for variants of the 2D and 3D Reeds–Shepp car with applications in image analysis. *Journal of Mathematical Imaging and Vision*, pages 1–33, 2018.
- [28] Carlos Esteves, Christine Allen-Blanchette, Ameesh Makadia, and Kostas Daniilidis. Learning $SO(3)$ equivariant representations with spherical CNNs. In *Proceedings of the European Conference on Computer Vision (ECCV)*, pages 52–68, 2018.
- [29] Lawrence C Evans. *Partial differential equations*, volume 19. American Mathematical Soc., 2010.
- [30] Albert Fathi and Ezequiel Maderna. Weak KAM theorem on non compact manifolds. *Nonlinear Differential Equations and Applications NoDEA*, 14(1-2):1–27, Aug 2007.
- [31] David J. Field, Anthony Hayes, and Robert F. Hess. Contour integration by the human visual system: Evidence for a local “association field”. *Vision Research*, 33(2):173–193, 1993.
- [32] Marc Finzi, Samuel Stanton, Pavel Izmailov, and Andrew Gordon Wilson. Generalizing convolutional neural networks for equivariance to Lie groups on arbitrary continuous data. In Hal Daumé III and Aarti Singh, editors, *Proceedings of the 37th International Conference on Machine Learning*, volume 119 of *Proceedings of Machine Learning Research*, pages 3165–3176. PMLR, 13–18 Jul 2020.
- [33] B. Franceschiello, A. Mashtakov, G. Citti, and A. Sarti. Geometrical optical illusion via sub-Riemannian geodesics in the roto-translation group. *Differential Geometry and its Applications*, 65:55–77, 2019.
- [34] Erik M Franken. *Enhancement of crossing elongated structures in images*. PhD thesis, Eindhoven University of Technology, 2008.
- [35] G. Medioni, M.-S. Lee, and C.-K. Tang. *Tensor Voting: A Perceptual Organization Approach to Computer Vision and Machine Learning*, volume 5 of *Synthesis Lectures on Image, Video, and Multimedia Processing*. Morgan and Claypool, 2011.
- [36] D. H. Hubel and T. N. Wiesel. Receptive fields of single neurons in the cat’s striate cortex. *Journal of Physiology*, 148:574–591, 1959.
- [37] Risi Kondor and Shubhendu Trivedi. On the generalization of equivariance and convolution in neural networks to the action of compact groups. In Jennifer Dy and Andreas Krause, editors, *Proceedings of the 35th International Conference on Machine Learning*, volume 80 of *Proceedings of Machine Learning Research*, pages 2747–2755, Stockholm, Sweden, July 2018. PMLR.
- [38] Alex Krizhevsky, Ilya Sutskever, and Geoffrey E Hinton. Imagenet classification with deep convolutional neural networks. In F. Pereira, C.J. Burges, L. Bottou, and K.Q. Weinberger, editors, *Advances in Neural Information Processing Systems*, volume 25. Curran Associates, Inc., 2012.

- [39] Yann LeCun, Bernhard Boser, John S Denker, Donnie Henderson, Richard E Howard, Wayne Hubbard, and Lawrence D Jackel. Backpropagation applied to handwritten zip code recognition. *Neural computation*, 1(4):541–551, 1989.
- [40] G. Litjens, B.E. Bejnodri, A.A.A. Setio, F. Ciompi, M. Ghafoorian, J.A.W.M. van der Laak, B. van Ginneken, and C.I. Sánchez. A survey on deep learning in medical image analysis. *Medical Image Analysis*, 42:60–88, December 2017.
- [41] I. Moiseev and Yu. L. Sachkov. Maxwell strata in sub-Riemannian problem on the group of motions of a plane, 2008.
- [42] Edouard Oyallon and Stéphane Mallat. Deep roto-translation scattering for object classification. In *Proceedings of the IEEE Conference on Computer Vision and Pattern Recognition*, pages 2865–2873, 2015.
- [43] Mercedes E. Paoletti, Juan M. Haut, Swalpa Kumar Roy, and Eligius M. T. Hendrix. Rotation equivariant convolutional neural networks for hyperspectral image classification. *IEEE Access*, 8:179575–179591, 2020.
- [44] J. Petitot. The neurogeometry of pinwheels as a sub-Riemannian contact structure. *Journal of Physiology - Paris*, 97:265–309, 2003.
- [45] R.Duits, B.Smets, E.J.Bekkers, and J.M.Portegies. Equivariant deep learning via morphological and linear scale space PDEs on the space of positions and orientations. *LNCS*, 12679:27–39, 2021.
- [46] Y.L. Sachkov. Cut locus and optimal synthesis in the sub-Riemannian problem on the group of motions of a plane. *ESAIM: Control, Optimization and Calculus of Variations*, 17:293–321, 2011.
- [47] Víctor Garcia Satorras, Emiel Hoogeboom, and Max Welling. E(n) equivariant graph neural networks. In Marina Meila and Tong Zhang, editors, *Proceedings of the 38th International Conference on Machine Learning*, volume 139 of *Proceedings of Machine Learning Research*, pages 9323–9332. PMLR, 18–24 Jul 2021.
- [48] Martin Schmidt and Joachim Weickert. Morphological counterparts of linear shift-invariant scale-spaces. *Journal of Mathematical Imaging and Vision*, 56(2):352–366, 2016.
- [49] Laurent Sifre and Stéphane Mallat. Rotation, scaling and deformation invariant scattering for texture discrimination. pages 1233–1240, 06 2013.
- [50] Bart M. N. Smets, Jim Portegies, Erik J. Bekkers, and Remco Duits. PDE-based group equivariant convolutional neural networks. *Journal of Mathematical Imaging and Vision*, Jul 2022.
- [51] A.F.M ter Elst and Derek W Robinson. Weighted subcoercive operators on Lie groups. *Journal of Functional Analysis*, 157(1):88–163, 1998.
- [52] R. van den Boomgaard and A. Smeulders. The morphological structure of images: the differential equations of morphological scale-space. *IEEE Transactions on Pattern Analysis and Machine Intelligence*, 16(11):1101–1113, 1994.
- [53] Maurice Weiler and Gabriele Cesa. General E(2)-equivariant steerable CNNs. In *Advances in Neural Information Processing Systems*, pages 14334–14345, 2019.
- [54] Maurice Weiler, Patrick Forré, Erik Verlinde, and Max Welling. Coordinate independent convolutional networks – isometry and gauge equivariant convolutions on Riemannian manifolds, 2021.
- [55] Maurice Weiler, Fred A Hamprecht, and Martin Storath. Learning steerable filters for rotation equivariant CNNs. In *Proceedings of the IEEE Conference on Computer Vision and Pattern Recognition*, pages 849–858, 2018.

- [56] M. Winkels and T.S. Cohen. 3D G-CNNs for pulmonary nodule detection. *MIDL*, pages 1–11, 2018. <https://arxiv.org/abs/1804.04656>.
- [57] D. Worrall and G. Brostow. CubeNet: Equivariance to 3D rotation and translation. *ECCV 2018*, pages 585–602, 2018.
- [58] Daniel Worrall and Max Welling. Deep scale-spaces: Equivariance over scale. In H. Wallach, H. Larochelle, A. Beygelzimer, F. d'Alché-Buc, E. Fox, and R. Garnett, editors, *Advances in Neural Information Processing Systems*, volume 32. Curran Associates, Inc., 2019.
- [59] Daniel E Worrall, Stephan J Garbin, Daniyar Turmukhambetov, and Gabriel J Brostow. Harmonic networks: Deep translation and rotation equivariance. In *Proceedings of the IEEE Conference on Computer Vision and Pattern Recognition*, pages 5028–5037, 2017.